Direct and semi-direct aerosol effects of Southern African biomass burning aerosol

Naoko Sakaeda[1], Robert Wood[1], and Philip Rasch[2]

[1]University of Washington, Seattle, USA

[2]Pacific Northwest National Laboratory, Richland, USA

Abstract

Direct and semi-direct radiative effects of biomass burning aerosols from Southern African fires during July-October are investigated using 20 year runs of the Community Atmospheric Model (CAM) coupled to a slab ocean model. Aerosol optical depth is constrained using observations in clear skies from MODIS and for aerosol layers above clouds from CALIPSO. Over the ocean, where the aerosol layers are primarily located above cloud, negative top of atmosphere (TOA) semi-direct radiative effects associated with increased low cloud cover dominate over a weaker positive all-sky direct radiative effect (DRE). In contrast, over the land where the aerosols are often below or within cloud layers, reductions in cloud liquid water path (LWP) lead to a positive semi-direct radiative effect that dominates over a near-zero DRE. Over the ocean, the cloud response can be understood as a response to increased lower tropospheric stability (LTS) which is caused both by radiative heating in overlying layers and surface cooling in response to direct aerosol forcing. The marine cloud changes are robust to changes in the cloud parameterization (removal of the hard-wired dependence of clouds on LTS), suggesting that they are physically realistic. Over land decreased LWP is consistent with weaker convection driven by increased static stability. Over the entire region the overall TOA radiative effect from the biomass burning aerosols is almost zero due to opposing effects over the land and ocean. However, the surface forcing is strongly negative requiring a reduction in precipitation. This is primarily realized through reductions in convective precipitation on both the southern and northern flanks of the convective precipitation region spanning the equatorial rainforest and the ITCZ in the southern Sahel. The changes are consistent with the low-level aerosol-forced cooling pattern. The results highlight the importance of semi-direct radiative effects and precipitation responses for determining the climatic effects of aerosols in the African region.

1. Introduction

The effects of aerosols emitted by biomass burning on Earth's radiation budget are significant but their magnitude and extent are not yet fully understood (Schultz et al. 2006; Ramanathan and Carmichael 2008). Southern Africa is a region characterized by intense biomass burning emissions during the months of June to October (Cooke et al. 1996). Biomass burning contributes to over 86% of the total global emissions of black carbon -soot, and the largest source of biomass burning emissions is the African savannas (Levine et al., 1995). These emissions form extensive aerosol layers which advect primarily westward over the southeastern Atlantic Ocean (e.g. Matichuk et al. 2007, Chand et al., 2009), where they overlay vast decks of stratocumulus clouds.

The reflection and absorption of solar radiation by aerosols changes the radiative balance of the lower atmosphere and may plausibly induce feedbacks on clouds and the hydrological cycle (e.g. Lau et al., 2006). Climate model studies have found that the climate sensitivity to absorbing aerosols such as black carbon can be two or more times larger than the sensitivity to carbon dioxide for a given top-of-atmosphere (TOA) radiative forcing (Hansen et al., 1997; Cook and Highwood, 2004). This is in part because, in addition to the aerosol direct effect, models show a reduction in cloudiness driven by the aerosol heating profile (Ackerman et al. 2000), a response termed the semi-direct aerosol effect (Hansen et al. 1997). Studies have also indicated that there may be important aerosol indirect effects associated with absorbing aerosols acting as cloud condensation nuclei that may partially cancel their warming effect (Chen et al. 2010).

Observations indicate that, for a given aerosol single scattering albedo, the direct radiative forcing efficiency (direct radiative forcing per unit of aerosol optical depth) depends primarily on the amount of cloud cover (Chand et al., 2009) since it is dependent on the albedo of the underlying surface (Chylek and Coakley 1974). Over the southeastern Atlantic, there is no consensus in the models as to the sign or magnitude of the direct aerosol forcing (Schulz et al. 2006), and this may be caused in part due to differences in the representation of clouds across models. Observationally-derived estimates, assuming plausible single scattering albedos, indicate that the aerosol TOA direct forcing over the southeastern Atlantic switches from positive to negative for regions where the cloud cover exceeds about 40% (Chand et al. 2009).

The semi-direct aerosol effect is caused by a change in cloud cover or cloud liquid water path due to heating from aerosol absorption of solar radiation. Morgan et al. (2006) found a lack of consensus as to the sign and magnitude of the global semi-direct effect among twenty-four expert atmospheric and climate scientists, while estimates of direct and indirect effects were more consistent among the experts. Unraveling the uncertainties in the semi-direct effects is important as some studies found that the magnitude of semi-direct effects could exceed the direct forcing (Johnson et al., 2004) and the atmospheric feedback processes that arise from semi-direct effect could play an important role explaining the total aerosol radiative effect (Lau et al., 2010).

Several studies have estimated semi-direct effects in global and regional scales (Hansen et al., 1997, Penner et al. 2003, Cook and Highwood 2004, Johnson et al. 2004; Allen and Sherwood 2010), but little consistency is seen among their results. Johnson et al. (2004) examined the dependence of the aerosol radiative effect on the vertical distribution of aerosols. They found that the sign of direct and semi-direct effects can be different depending on whether absorbing aerosol is located above, in, or both in and above the boundary layer. Other studies

(Cook and Highwood, 2004; Yoshimori and Broccoli 2008, Sud et al., 2009; Allen and Sherwood, 2010) also recognize the dependence of the vertical distribution of aerosols on the radiative forcing. It is also known that the semi-direct effect estimated from modeling studies is dependent on the cloud scheme of the models (Cook and Highwood, 2004; Williams et al., 2004). There is a lack of plausible hypotheses for how clouds respond to absorbing aerosols, and numerous questions remain. For example, to what extent might reductions in downwelling solar radiation impact clouds underlying aerosol layers, compared with changes in the lower tropospheric static stability that are observed to impact cloud cover (Klein and Hartmann 1993, Wood and Bretherton 2006)? Can static stability metrics derived primarily from regions without aerosol layers offer useful guidance as to the response of low clouds to overlying absorbing aerosols? Or do the changes in the large scale atmospheric circulation (e.g. vertical velocity) induced by aerosol heating also play a major role in driving cloud responses?

In this study, we use a global atmospheric model coupled with a slab ocean to assess the aerosol direct and semi-direct radiative effects at the regional scale associated with carbonaceous aerosols emitted by southern African biomass burning. A global model is used because regional simulations that restrict advection at the boundaries may lead to unrealistic or amplified results (Sud et al. 2009). We choose to examine a limited regional system where the configuration of aerosols and clouds is fairly simple and yet the scenarios are realistic compared with idealized models. Global studies, while all-encompassing, have the limitation of inclusion of a whole host of different aerosol-cloud configurations which renders understanding the responses more difficult. We conduct simulations with and without carbonaceous aerosols to derive the aerosol direct and semi-direct effects. We break down the aerosol direct radiative effect (DRE) into that

97 for clear sky and cloudy sky, and the semi-direct effect into components caused by changes in
98 cloud cover and liquid water path separately.

99 Section 2 describes the numerical experiments performed, and uses observations to
100 constrain the aerosol properties used in the model. Section 3 describes the results of the
101 simulations, while Section 4 presents a discussion and conclusions.

102 2. Experiments and set-up

103 We use NCAR's global atmospheric model, the Community Atmospheric Model (CAM) Version
104 3.0 - Slab Ocean Model (CAM3-SOM) to interpret the impact of biomass burning aerosol layers
105 at the regional scale. Our study focuses on the examination of direct and semi-direct effect and
106 therefore this model does not include aerosol indirect effects. The cloud nucleating properties of
107 biomass burning aerosols may be important (Chen et al. 2010), but we do not consider these
108 effects here since CAM Version 3.0 does not resolve aerosol activation. In addition, over the
109 ocean many of the aerosol layers are not in direct contact with the underlying cloud layers which
110 would imply weaker indirect effects than one might observe elsewhere.

111 Aerosol fields are provided to the model rather than emissions, and are derived using the
112 method of Collins et al. (2001) and Rasch et al. (2001) which uses the Model for Atmospheric
113 Chemistry and Transport (MATCH) (Rasch et al., 1997) a chemical transport model to produce
114 model fields that are then adjusted to give approximate agreement with satellite observations (see
115 Section 2.1 below). The model aerosol species are natural and anthropogenic sulfate, sea-salt,
116 organic and black carbon, and dust. The aerosols are annually-cyclic monthly values. Additional
117 details are provided in the CAM Science Description document (Collins et al. 2004).

Two 20-year simulations are performed: one (termed PD) with present day aerosol fields and another (termed NC) in which all the carbonaceous aerosols (organic and black carbon) are removed over the region 10°N-30°S, and 20°W-50°E (see map Fig. 1) during the main southern African biomass burning season (July-October). During the other months when the effect of biomass burning from southern Africa is minimal, the aerosols in the two simulations are set to present day levels. The carbonaceous aerosol fields in the present day simulation are taken from the MATCH model and we found that while the geographic distribution of the aerosol optical depth matched satellite observations well, better quantitative agreement was obtained by doubling the organic and black carbon masses over the region 10°N-30°S, and 20°W-50°E. Comparisons of the model and satellite-derived aerosol fields are discussed in the next section.

2.1 Constraining the model aerosol fields with observations

To constrain the aerosol fields used in the model, we use data from both the Moderate Resolution Imaging Spectroradiometer (MODIS), and from the Cloud Aerosol Lidar and Infrared Pathfinder Satellite Observation (CALIPSO). From MODIS we use clear-sky passive visible retrievals (Remer et al. 2005) of aerosol optical depth (AOD) at a wavelength of 500 nm, and of the fine mode aerosol fraction. These retrievals include improved estimates over land (Levy et al. 2007), although there are still problems over bright surfaces. We use Collection 5 of the MOD04 aerosol product as included in the Level-3 MODIS Atmosphere Daily product gridded to 1×1°, and from this we create a July-October mean (2001-2008) clear-sky AOD climatology (Fig. 2) for all aerosols and for the fine mode separately.

In addition, we use active spaceborne lidar observations from CALIPSO to estimate the AOD at 532 nm of aerosol layers above clouds using the retrieval method of Chand et al. (2008).

We use two years of data (2006 and 2007) to create estimates of the mean AOD of elevated aerosol layers above low clouds, following the methodology described in Chand et al. (2009). Figure 2 shows maps of mean total (fine+coarse) AOD at ~500 nm for all-sky from CAM (PD simulation), for clear-sky from MODIS, and for aerosol layers above clouds from CALIPSO. We additionally screen MODIS AOD for days where cloud fraction was less than 0.5 to reduce contamination from the effects of broken clouds (see e.g. Kaufman et al. 2005, Loeb and Manalo-Smith 2005). Good agreement of the spatial pattern of AOD is seen between the aerosol fields from the CAM and from the observations (Fig. 2).

We compare the fields using regression and mean values for the region with CALIPSO observations (7.5°N-22.5°S, 27.5°W-17.5°E). For the spatial correlation, r=0.87 between CAM and MODIS total AOD and r=0.74 between CAM and CALIPSO. The mean MODIS total AOD over ocean is 0.26 (vs 0.38 over land) while it is 0.24 (vs 0.40 over land) for CAM, indicating that our adjustment of the CAM fields produces a good match with the observations over both ocean and land. The CALIPSO AOD estimates are smaller (see Fig. 2c), but this is expected since CALIPSO retrieval used here only captures those aerosol layers that lie above clouds, and the CAM aerosol fields indicate that there are carbonaceous aerosols both above and below clouds over the ocean. In addition, data from CALIPSO (Chand et al. 2008) indicates that the aerosol layers above clouds have high Angstrom exponents of ~2, and so a fairer test of the fidelity with which biomass burning aerosol is represented in the model would be to compare CAM AOD from carbonaceous aerosols with MODIS fine mode AOD. These compare extremely well (Fig. 2d and 2e, and Fig. 3), with mean values over ocean (land) of 0.16 (0.23) for MODIS fine mode AOD and 0.14 (0.27) for CAM carbonaceous aerosols. Recalling the lower AOD for aerosols above clouds from CALIPSO (Fig. 3, with means of 0.09 and 0.13 over

ocean and land respectively), it is reasonable to conclude that perhaps 50-75% of the fine mode AOD over the ocean in regions influenced by carbonaceous aerosols is coming from layers above clouds. The ratio of the mean AOD from CALIPSO to that from the MODIS fine mode is 0.56 over ocean (see also Fig. 3). This is consistent with the model vertical aerosol structure: a longitude-height cross section of cloud occurrence and carbonaceous aerosols averaged over 0-20°S from the CAM (Fig. 4a) shows that the carbonaceous aerosols peak near the surface over land but the majority of the mass loading is above the low clouds in the marine boundary layer (MBL) over ocean (Fig. 4b gives mean ocean profiles). This is also in agreement with in-situ aircraft observations made over the ocean in this region (Anderson et al. 1996) which show a peak in fine mode aerosols at 3-4 km altitude and considerably lower aerosol concentrations close to the surface. This configuration of aerosols being primarily above the clouds over the ocean to the west of southern Africa is a result of prevailing winds in the MBL over the ocean mainly bringing relatively clean air from the south while the winds at 850 hPa and above are advecting aerosols from the South African continent (see also Matichuk et al.2007, Chand et al. 2009).

2.2 Partitioning the radiative response into direct and semi-direct components

Differences between the PD and NC simulations are used to examine the effects of the biomass burning smoke on the radiative budget and regional climate. Here, we focus on the months of July to October, so all quantities we present are means over this period. We only consider shortwave effects here since the longwave effects of the changes in aerosols and the responses they incite in low clouds are small. Each of the simulations is run with an offline calculation of the aerosol direct radiative effect (DRE), which allows us to parse the total change in net solar irradiance (at an arbitrary level and horizontal location) ΔF into four terms:

$$\Delta F = \{DRE_{CLR}(1-\overline{CF})\} + \{\overline{CF}\cdot DRE_{CLDY}\} + \{\overline{CF}\cdot \Delta F_{CLDY,LWP}\} + \{\Delta CF(\overline{F}_{CLDY} - \overline{F}_{CLR})\} \quad [1]$$

D1 D2 S1 S2

Throughout, the symbol Δ represents the difference between the two simulations (PD - NC), and F is the net solar irradiance. A derivation of [1] is given in Appendix A. The first term in Eqn. [1], D1 $\{DRE_{CLR}(1-\overline{CF})\}$ is the aerosol direct radiative effect in clear sky conditions weighted by the fractional clear sky amount. The second term, in Eqn. [1], D2 $\{\overline{CF}\cdot DRE_{CLDY}\}$ is the aerosol direct radiative effect in cloudy-sky conditions weighted by cloud fractional amount. The sum of these two terms is the total aerosol direct radiative effect. The third term, S1 $\{\overline{CF}\cdot \Delta F_{CLDY,LWP}\}$ is the semi-direct aerosol effect in cloudy sky conditions associated with changes in the cloud liquid water path (LWP). The fourth term, S2 $\{\Delta CF(\overline{F}_{CLDY} - \overline{F}_{CLR})\}$ represents the semi-direct aerosol effect due to cloud cover change. The semi-direct aerosol effects in this study are a result of changes in the radiative heating profile and their effects on meteorological fields forced by presence of carbonaceous aerosols. Since we are using a slab ocean model, these meteorological changes include those stemming from surface temperature reductions due to reduced solar irradiance. Cloudy-sky solar flux is calculated in the standard way from the model outputs using shortwave cloud radiative effect (SWCRE) and the difference between the clear sky and all-sky solar fluxes. The sum of the third and the fourth terms represents the total aerosol semi-direct radiative effect. We calculate and examine these terms at the top of atmosphere and at the surface, and the difference between them constitutes the atmospheric aerosol radiative effect.

We also define a radiative forcing efficiency by carbonaceous aerosols as the forcing ΔF (or term in [1] contributing to ΔF) per unit of carbonaceous aerosol optical depth (i.e. the difference in AOD between the PD and NC model runs), which has units of $Wm^{-2}\tau^{-1}$.

3. Results

3.1 Regional maps of aerosol radiative effects

Table 1 and Fig. 5 provide details of the time-mean (July-October) shortwave radiative effects (flux differences) due to carbonaceous aerosols, averaged over the region for which the aerosol perturbations have been applied, i.e. 20°W-50°E, 10°N-30°S (see Fig. 1). Table 1 gives mean, median and spatial standard deviation of the aerosol radiative effect and contributing terms (i.e. D1, D2, S1 and S2) at the TOA, the surface and for the atmosphere, broken down by ocean,land, and ocean+land respectively. Figure 5 presents maps of these terms including the sum total of all the effects.

3.2 Direct radiative effects and efficiency

Negative top of atmosphere clear-sky DRE (term D1) indicates that over dark surfaces aerosol scattering dominates (Fig. 5a). Over the region of high surface albedo such as around the Kalahari Desert in southern Africa (Fig. 5a), high surface albedo leads to weak positive clear-sky DRE at the TOA. Over the ocean, because there are extensive low clouds, the magnitude of term D2 (cloudy-sky DRE weighted by cloud cover) exceeds term D1 in the mean (Table 1). Term D2 is positive because the clouds are sufficiently bright, and the aerosol absorption sufficiently strong (Fig. 3k,l), and agrees with observationally-derived satellite estimates constrained with in-situ aerosol single-scattering albedo (Chand et al. 2009). However, the cancellation between

terms D1 and D2 in the mean over the ocean belies a highly spatially variable signal in cloudy-sky DRE (term D2, Fig. 5b) compared with D1 (Table 1). Term D2 greatly exceeds D1 over the region where there is both extensive low cloud cover and carbonaceous aerosols (Figs. 1, 2 and Fig. 10). In this region close to the southern African coast the carbonaceous aerosol layers are primarily located above low clouds (Fig. 4) which maximizes the effects of aerosol absorption and leads to a strong positive DRE at the TOA.

Over land, the TOA DRE terms are smaller than over ocean, but there is more or less complete cancellation of terms D1 and D2 leading to near-zero DRE. This is interesting given that the low cloud cover is much smaller over land than over ocean (Fig. 6). However, there is considerable total cloud over the land (almost 50%, see Table 1), much of which is in the form of thin cirrus. Satheesh (2002) uses radiative transfer calculations to show significant positive DRE at the TOA even the case where clouds with an optical thickness of 4 are above absorbing aerosols. The TOA DRE would become more positive still for optically thinner clouds.

The atmospheric aerosol radiative effect (i.e. the difference between TOA and surface) comes almost exclusively from the DRE (Table 1 and Fig. 5k-n), which is strongly positive due to aerosol absorption of solar radiation. The clear sky, atmospheric DRE (not weighted by clear sky amount) linearly increases with AOD ($r = 0.97$). The cloudy sky atmospheric DRE has a maximum where low cloud fraction has its relative maximum (Fig. 5l). This further emphasizes the importance of low clouds underlying the absorbing aerosol layers.

The DRE at the surface is strongly negative (Table 1 and Fig. 5f,g) and is dominated by the clear sky contribution over the land. Over ocean, there are approximately equal contributions from the clear and cloudy sky, which is interesting and has potentially important implications for

248 the impacts on the upper ocean heat budget, which can feed back and impact the semi-direct
249 effects.

250 Because the aerosol DRE is approximately linearly dependent on aerosol optical depth
251 (Chylek and Coakley, 1974), the dependence of the DRE on other aerosol and cloud properties
252 can be efficiently examined using the concept of radiative forcing efficiency (RFE, the radiative
253 effect per unit of AOD change between the PD and NC simulations). Maps showing the total
254 direct RFE (sum of terms D1+D2 per unit of carbonaceous aerosol optical depth) for the TOA,
255 surface, and the atmosphere are shown in Fig. 6. Consistent with Chand et al. (2009), there is a
256 high correlation between mean low cloud fraction and total direct RFE for both the atmosphere
257 and TOA over ocean (r=0.84 for RFE at the TOA and r=0.79 for the atmospheric RFE). The
258 correlation is weaker over land (r values of 0.73 and 0.66 for the TOA and atmosphere
259 respectively), but is still strong, highlighting the important role that clouds play in determining
260 the DRE of biomass burning aerosols. In contrast, the correlation of the direct RFE at the surface
261 with low cloud cover is strong over land (r=0.92) while no significant correlation is found over
262 ocean (r=0.17), a point to which we return below.

263 For the atmospheric absorption, the two key factors that contribute to the land-ocean
264 contrasts are the vertical profile of aerosols relative to cloud height and the albedo of the surface
265 underlying the aerosol layer. Figure 7 shows a contrasting dependence of total atmospheric direct
266 RFE as a function mean low cloud fraction. When clouds are primarily found above aerosol
267 layers, the total atmospheric absorption RFE weakens with cloud cover, whereas it strengthens
268 when aerosol layer are primarily above clouds. Since aerosol layers are primarly found above
269 clouds over ocean and in/below clouds over land (Fig. 4), the atmospheric direct RFEs over
270 ocean and land have opposing dependencies on low cloud cover. When the absorbing aerosols

271 are in and below the low clouds, the aerosol absorption of solar radiation is weaker because
272 clouds reflect a significant fraction of the incoming solar radiation before it can reach the aerosol
273 layer. However when the absorbing aerosols are above clouds, aerosol absorption is stronger
274 with more low cloud cover because reflection from clouds gives the aerosols a second
275 opportunity to absorb solar radiation.

276 As mentioned above, the surface direct RFE is poorly correlated with low cloud cover
277 over ocean (r=0.17), but is well-correlated with cloud LWP (r=0.79) indicating that thick low
278 clouds shield the ocean surface from the radiative effects of aerosols since high LWP regions are
279 those with the weakest negative surface RFE (Fig. 6). Over land, the surface direct RFE is well
280 correlated with low cloud cover and liquid water path, but since low cloud fraction and cloud
281 liquid water path over land are tightly coupled (r=0.85), it seems reasonable to suggest that it is
282 the thickness of the cloud that is the primary control on the surface direct RFE over land as it is
283 over ocean.

284 Over land, clear sky direct RFE at the TOA is highly dependent on surface albedo.
285 Surface albedo explains almost 90% of the variance in clear sky direct RFE at TOA over land
286 and the critical surface albedo where the direct RFE changes its sign is 0.23±0.01. All-sky direct
287 RFE at the TOA becomes less negative as low cloud cover increases over both land and ocean.
288 Over land, where the aerosols are mainly in and below the low clouds, the positive atmospheric
289 DRE weakens with increasing low cloud fraction at about half of the rate the negative surface
290 DRE weakens. Therefore the all-sky RFE at the TOA, which is the sum of the surface and
291 atmospheric RFE, increases with low cloud cover. The total direct RFE increases with low cloud
292 cover over the ocean as well, but the mechanism is different than that over land. Since the albedo
293 of sea surface is low, the aerosol reflection of solar radiation leads to negative RFE at the TOA

where cloud cover is low. However as the low cloud cover increases, absorption of solar radiation due to the aerosol layers above the clouds reduces the radiation going out at TOA and leads to positive RFE.

Over the ocean, the linear slope of the all-sky direct RFE at the TOA against low cloud cover (Fig. 8) is similar to that from observationally-derived estimates of Chand et al. (2009). Chand et al. (2009) used an observational data of aerosol optical depth for layers above clouds from CALIPSO, together with MODIS-derived cloud optical thickness, to run a radiative transfer model to estimate the mean direct radiative effect of elevated aerosol layers above regions with partial cloudiness. Most land regions were excluded from the Chand et al. analysis, so their results should be compared to our results over ocean. The TOA direct RFE over ocean increases from -33 to +43 W m^{-2} as low cloud fraction increases from zero to unity in the model (Fig. 8), compared with -35 to +51 W m^{-2} in Chand et al., in good agreement. The TOA results, however, mask the fact that there are considerable differences in the surface and atmospheric direct RFE low cloud trends (Fig. 8) which largely offset each other. Specifically, we find that the increase of the atmospheric direct RFE with cloud fraction in the model is approximately twice as large as that from Chand et al. (2009), while the model surface direct RFE increases much more weakly with cloud cover in the model compared with the observations. Overall, the model atmospheric direct RFE is lower than that found in Chand et al. (2009). Some of this behavior may be explained by the fact that the Chand et al. study only considered aerosol optical depth above clouds while our simulations incorporate the effects of aerosols regardless of position in the vertical column. The observational methodology would therefore be expected to enhance the effects of clouds on the atmospheric absorption compared to cases where the aerosols are sometimes in or below clouds as they are in the model (and in reality). On the other

hand, the largest discrepancies are found for low cloud fraction suggesting that the aerosol single scattering albedo is also responsible. We note that the single scattering albedo in the model (see e.g. Fig. 9) is typically higher than the value of 0.85 assumed in Chand et al. (2009). The lack of accurate single scattering albedo observations for these aerosol layers is a significant impediment to our understanding of their radiative effects.

Another factor that might affect differences between the model and observationally-derived RFEs is that the model single-scattering albedo (SSA) has spatial variability whereas in Chand et al. (2009) it was assumed constant (SSA=0.85, consistent with the mean from surface-based observations over southern Africa, Leahy et al. 2007). The discrepancies between the model and observationally-derived direct RFEs may therefore not entirely be due to a poor model representation of the aerosol direct effects. Chand et al. (2009) found a dependence of the critical cloud fraction (CF*, the cloud fraction at which total direct RFE at the TOA changes its sign from negative to positive) on aerosol SSA. Since direct $RFE_{ALL\text{-}SKY}=(1\text{-}CF)\times RFE_{CLR}+CF\times RFE_{CLDY}$, the critical cloud fraction CF* is derived by setting $RFE_{ALL\text{-}SKY} = 0$, to give

$$CF^* = \left(\frac{RFE_{CLR}}{RFE_{CLDY}} + 1 \right)^{-1} \quad [2]$$

Over ocean where surface albedo is universally low, we use linear regression of the direct TOA RFE_{CLR} and RFE_{CLDY} against aerosol SSA from the model to give a curve of CF* against SSA. The aerosol SSA used here is the AOD-weighted mean from the PD and NC simulations. The correlation coefficients for TOA RFE_{CLR} and RFE_{CLDY} against the mean aerosol SSA are

0.74 and 0.16 respectively. Figure 9 shows that this derived function separates regions of positive and negative all-sky TOA direct RFE fairly well even though it contains a significant error range due to low correlation between cloudy sky direct RFE and aerosol SSA. As the aerosols become more absorbing (lower SSA), the critical cloud fraction reduces from ~0.7 for SSA=0.96 to ~0.33 for SSA=0.86. Alternatively, from Fig. 8 we can infer that CF* is ≈0.44 over ocean for the region as a whole. Chand et al. (2009) found that CF*≈0.4 for SSA=0.85, which is a little higher than for the model simulations (at the same SSA), although the model SSA is in most places higher than that assumed in the observational analysis, which leads to a slightly higher CF* for the model as a whole. We think that this is because the model-derived SSA includes aerosol species other than carbonaceous aerosols which are likely to be less absorbing. Nevertheless, the dependence of CF* on the aerosol SSA is consistent with that found in the observational analysis (see supplementary material for Chand et al. 2009), and these findings give us some confidence that the configuration of aerosol and cloud fields in the model are a reasonably faithful representation of reality.

3.3 Semi-direct radiative effects

Table 1 shows that the semi-direct radiative effects at the TOA have magnitudes comparable to the direct radiative effects, and therefore play an important role in determining the net forcing at TOA. However, there are important land-ocean contrasts in the semi-direct effects. Cloud responses over the ocean (Table 1) are dominated by *increases* in cloud cover (with little LWP change), while land responses are dominated by *reductions* in LWP (with little cloud cover change). We will examine reasons for the cloud changes in the following sections. It is also important to note that the semi-direct atmospheric radiative effect (Figs. 5m,n) indicates that changes in cloud cover and LWP have only small effects on the shortwave absorption in the

361 atmosphere compared with the absorption by aerosols themselves. Thus, the surface and TOA
362 semi-direct effects are almost equal (Table 1).

363 The mean semi-direct effect at the TOA is positive over the land (+1.3 W m^{-2} for LWP
364 and cloud fraction effects combined, see Table 1) and negative over the ocean (-2.6 W m^{-2}). The
365 strong land-ocean differential is consistent with a recent climate model study (Allen and
366 Sherwood 2010) but whereas we find significantly negative TOA semi-direct effect over the
367 ocean, Allen and Sherwood (2010) find almost zero oceanic semi-direct effect for the globe as a
368 whole. However, our analysis is focused on a limited region where over most of the oceanic
369 regions the aerosols overlay clouds.

370 The spatial patterns of semi-direct effects (Fig 5c,d) are generally more variable than
371 those for the DRE indicating a complexity in the cloud responses in the model which includes
372 nonlocal feedbacks. Over the ocean the TOA semi-direct radiative effect due to cloud cover
373 changes provides a significant offsetting of the cloudy sky direct radiative effect (compare Figs.
374 5b,d) and not surprisingly these effects maximize off the Angolan coast (5-15°S) where the
375 carbonaceous AOD is maximal (see Fig. 1) and the cloud cover is large (Fig. 10). Over the land,
376 the TOA semi-direct effect adds to the positive cloudy sky DRE, making the impact of clouds on
377 the total radiative effect at the TOA significantly positive.

378 Interestingly, the total TOA radiative effect (sum of terms D1, D2, S1, and S2) is almost
379 equal and of opposite sign over the ocean and land. Since the land cover in our focus region is
380 slightly less than 50%, this indicates that the total TOA radiative effect for the region as a whole
381 is close to zero.

382 The semi-direct radiative forcing efficiency SRFE can be defined analogously to the
383 direct RFE as the sum of terms S1 and S2 in Eqn. 1 per unit of AOD change between the PD and

NC simulations. As with the direct RFE we calculate the SRFE at the surface, for the atmosphere, and at the TOA. However, since we find that the atmospheric semi-direct radiative forcing is very small, factors controlling the TOA and the surface SRFE are essentially one and the same (compare Figs. 5c,h and 5d,i), which simplifies the analysis. We do not study the longwave component of the semi-direct effects in this paper but note that because the model cloud changes are primarily associated with low clouds, we anticipate these effects to be quite small.

The SRFE in general is related to changes both in cloud fraction and cloud LWP, as would be expected since we already saw above that significant semi-direct effects are associated with changes in these parameters (Table 1 and Fig. 5). Over the land, where the changes in cloud fraction ΔCF between the PD and NC simulations are quite small (Table 1), the SRFE is well-correlated with the change in LWP, with generally decreasing LWP leading to positive SRFE almost everywhere. The correlation coefficient between SRFE and ΔLWP is r = -0.87 over land. For both land and ocean taken together, we use multiple linear regression of SRFE against ΔCF and ΔLWP which gives a multiple regression coefficient r = 0.78. However, we actually find that the semi-direct radiative effect itself (rather than the efficiency) is better multiply correlated with ΔCF and ΔLWP with a regression coefficient r = 0.85. This indicates that the changes in low clouds driven by the carbonaceous aerosols are not simply a function of the carbonaceous aerosol loading itself, but may be displaced in space most likely due to feedback processes that amplify the initial response. For example, whereas the heating of the troposphere due to the addition of absorbing aerosols would be expected to be more or less linearly related to the aerosol loading, the surface temperature response (itself a key determinant of the change in stability that might be expected to force cloud changes) will depend upon the surface direct RFE which is not simply a

function of aerosol loading (see Fig. 6a and associated discussion in Section 3.2). We will examine further the causes of the cloud responses in Section 3.4.

3.4 What drives the model cloud responses?

The model cloud responses to carbonaceous aerosols that constitute the semi-direct effects appear to be largely driven by increased lower tropospheric stability (LTS), which is typically defined as the difference in potential temperature between 700 hPa and the surface (see e.g. Klein and Hartmann 1993). Increased LTS is caused both by increased atmospheric heating and surface cooling from the absorbing aerosols. There is a good physical basis for expecting that LTS increases over the ocean would drive increases in low cloud cover by increasing the inversion strength, suppressing cloud vertical extent and maintaining a well-mixed boundary layer (Klein and Hartmann 1993, Wood and Bretherton 2006). Nevertheless, these previous studies are not focused on clouds driven by aerosol-driven stability changes, but by stability changes driven by continent-atmosphere dynamics (Richter and Mechoso 2004, 2006, Takahashi and Battisti 2007). It is therefore useful to understand the extent to which the aerosol-driven cloud and stability changes resemble those driven by other processes.

3.4.1 Sensitivity to model cloud scheme

Three types of clouds are diagnosed by the cloud scheme in CAM3: marine stratus, convective, and layered clouds (Boville et al. 2006). The cloud scheme is described in some detail in the CAM3 documentation[1]. Marine stratus cloud fractional cover is computed using the empirical linear relationship (the "Klein-line") with lower tropospheric stability (LTS) derived from observations by Klein and Hartmann (1993). The diagnosed marine stratocumulus cloud

[1] Available online at *http://www.cesm.ucar.edu/models/atm-cam/*

fraction is assigned to a layer below the layer of maximum static stability (inversion) and its amount is limited to be equal to the relative humidity within this layer. The total cloud fraction for a given layer is the sum of convective cloud and the maximum of the layered cloud and stratocumulus cloud fractions. Layered clouds are computed from the gridbox mean relative humidity, which has to exceed a pressure (i.e. height) dependent threshold (Boville et al. 2006). In order to assess the impact of the stability-based parameterization on determining the low cloud fraction and the importance of changes in these clouds for the semi-direct aerosol radiative effects, two more sets of simulations were performed, each of which PD and NC aerosols but where the Klein-line is not used in the determination of low clouds. We refer to these additional simulations as cloud scheme modification CLDMOD1 and CLDMOD2, and the one without any cloud modification CONTROL for this section.

The first set of simulations (call this CLDMOD1) –with and without carbonaceous aerosols, is run with the stability-based marine stratus cloud parameterization formula turned off. In the other words, the stratus cloud fraction is always computed from the maximum relative humidity in the layer below inversion. Comparison of stratus cloud fraction from these simulations with the original simulations without any cloud scheme modification showed that about 40-43% of the time stratus cloud computed from the stability-based parameterization does not exceed the maximum relative humidity within the layer and about 42% of the time they are equal. This indicates that there are only about 15-18% of the time the stability-based parameterized stratus cloud does not exceed the maximum relative humidity within a layer, which means that stratus cloud fraction in the CONTROL simulation is largely controlled by the Klein-line in our region of interest.

Then another set of simulations (termed CLDMOD2) is run neglecting the stratus cloud entirely in the computation of total cloud fraction in order to see the importance of stratus cloud on the carbonaceous aerosol radiative forcing. In other words, total cloud fraction is always computed as the sum of convective and layered cloud. Low cloud fraction in the PD or NC simulation with the cloud scheme modification CLDMOD2 is highly correlated ($r = 0.99$) with that in the CONTROL simulation over land, as expected since the model produces almost no stratus over land. However, over ocean the low cloud fraction is everywhere decreased by neglecting stratus cloud (CLDMOD2) in the computation of total cloud fraction, indicating that stratus cloud fraction is generally greater than layered cloud fraction in this region. However, the correlation of mean low cloud fraction between the CONTROL and CLDMOD2 modification remains quite high ($r^2 = 0.73$) demonstrating that even without the Klein and Hartmann diagnostic parameterization, the model is able to reproduce the geographical variability in mean low cloud cover over the ocean quite skillfully

Statistically significant differences are seen between CLDMOD2 and CONTROL in terms of the *change in low cloud fraction* due to carbonaceous aerosols (i.e. PD-NC). Even over land where the model produces almost no stability-based low cloud, change in low cloud fraction due to the aerosols is different in both magnitude and spatial pattern, which indicates that changes in the atmospheric circulation associated with changes in the cloud scheme are important. That is, the effect of the cloud scheme changes are not solely local, but involve teleconnections associated with changing surface temperatures. This has been noted before in simulations of the tropical Pacific where adjustments to low clouds in the stratocumulus region over the cool part of the ocean effected changes throughout the rest of the basin (Ma et al. 1996, Gordon et al. 2000). We do not explore this further in this manuscript.

473 Over ocean, the magnitude of the low cloud fraction changes due to carbonaceous
474 aerosols are generally reduced over ocean when the KH parameterization is not used (see Table
475 3), but the sign of the changes remains the same, This is also the case for the changes in cloud
476 LWP, and thus the semi-direct effects are also reduced to around 60% of their values when the
477 KH parameterization is included. Therefore, while the magnitude of the semi-direct effect is
478 uncertain, the sign is not simply a built-in response to free-tropospheric heating associated with
479 the diagnostic KH parameterization. Although this does not assure that the modeled cloud cover
480 responses over the ocean are consistent with the real-world responses, it does add credibility to
481 the results suggesting oceanic increases in low clouds. Figure 11 shows the changes in low cloud
482 fraction against those in LTS driven by carbonaceous aerosols for the KH and CLDMOD2. As
483 might be expected, the spatial correlation between changes in low cloud fraction and lower
484 tropospheric stability over ocean is reduced (r^2 reduced from 0.64 with KH to 0.35 without it),
485 but for most of the regions where the LTS increases most markedly, the low cloud cover also
486 increases regardless of which parameterization is adopted. This gives us some confidence that
487 the sign of the model cloud changes over ocean, both in terms of cloud fraction and cloud liquid
488 water path, are robust with respect to changes in the way in which low clouds are parameterized.
489 Since a large fraction of the total TOA aerosol radiative effect (sum of terms D1, D2, S1 and S2)
490 is associated with the semi-direct effects (Table 3) the total TOA radiative effect due to the
491 carbonaceous aerosols is roughly halved by removing the KH parameterization Thus, there
492 remains considerable uncertainty regarding the magnitude of the aerosol effects associated with
493 the parameterization of low clouds. The spatial pattern of thetotal aerosol effect at the TOA is
494 altered but the effects with and without the KH parameterization are still quite well correlated
495 over ocean and over land (Table 3). In contrast, at the surface and for the atmosphere the total

radiative forcing is not largely effected by the stratus cloud parameterization since the majority of the total radiative forcing comes from direct forcing.

3.4.2 Lower tropospheric meteorological changes over ocean

Low cloud cover changes (PD – NC) over the ocean are significantly correlated with LTS changes (Fig. 11), and these changes approximately follow those expected from the Klein and Hartmann (1993) relationship, with cloud cover increasing at approximately 0.05 per 1 K of ΔLTS (Fig 11).

The low cloud cover increases from NC to PD over the ocean despite the specific humidity *decreasing* in the cloud layer. Unlike the situation seen in Perlwitz and Miller (2010) where cloud cover increased due to increase in specific humidity exceeding the temperature warming, we find low cloud cover increases in our simulations are associated with a cooling of the marine boundary layer (Fig. 12) which leads to saturation specific humidity decreases that are greater than the decrease in specific humidity, resulting in an increase in relative humidity (Fig 14). The surface temperature cools (Fig. 12), and the surface latent heat flux reduces, because of the strong negative surface radiative effect (Table 1 and Fig 5), which is primarily a result of direct radiative effects (Table 1). However, although surface cooling is the primary driver of LTS increases, it is not the only driver, since the lower free-troposphere warms (Fig. 13a) by absorption of solar radiation by aerosols which reside primarily above cloud over the ocean (Fig. 4).

Another factor that might influence the marine low clouds is the significant change in large scale vertical velocity caused by the aerosol absorption in the lower troposphere. Figure 13d shows that the carbonaceous aerosols reduce the subsidence by as much as 20-30% in the height range 0.5-4 km in the region of heaviest carbonaceous aerosol loading. In response, the

519 model MBL deepens (Fig. 13b,c indicates that the drop-off in relative humidity and the cloud
520 fraction both move upwards). Over regions of the ocean not strongly impacted by biomass
521 burning, deeper boundary layers tend to be accompanied by *decreased* cloud cover (e.g. Wood
522 and Hartmann 2006), and so it seems reasonable to suppose that, given this forcing alone, the
523 cloud cover would decrease in response to the carbonaceous aerosol. The fact that this does not
524 happen suggests that the effect of increased stability overwhelms that of reduced subsidence.
525 Apart from changes in LTS and the large scale vertical velocity over ocean, we might
526 expect that reduced downwelling solar radiation at cloud top associated with absorption and
527 scattering from the aerosols aloft might enhance the net (LW+SW) cloud top cooling which
528 would drive thicker or more extensive clouds. We can crudely estimate the potential for this
529 effect as being proportional to the diurnal reduction in low cloud fraction associated with the
530 diurnal cycle of downwelling solar flux. Given this assumption, the expected low cloud cover
531 increase due to the aerosol-induced reduction of cloud-top downwelling solar flux reduction is
532 only 0.0035, which less than one fifth of the actual modeled overall low cloud fraction increase
533 (0.02) due to the aerosol effects (see Table 1). Therefore, we conclude that the great majority of
534 the low cloud cover increase is associated with factors other than reduced solar burn-off.

535 *3.4.2 Lower tropospheric meteorological changes over land*

536 Over the land, there are substantial reductions in cloud liquid water, but the low cloud
537 cover changes are minimal (Fig. 10). The low cloud cover is quite small over the land, since the
538 clouds are predominantly cumuliform, but the clouds extend to higher levels in the vertical
539 compared with the marine clouds. The increased stability is associated with low level cooling
540 and warming aloft. This appears to reduce the vertical transport of moisture by suppression of
541 shallow convection (Fig. 14) resulting in a moister surface and a drier and warmer troposphere

above this, especially between at altitudes 2-3 km where the aerosol heating is strongest. The reduction in shallow convection is the reason why the cloud liquid water path decreases over land. These results are in accordance with cloud resolving and GCM modeling studies showing that absorbing aerosols tend to suppress cloud when the heating is within the cloud layer itself (Ackerman et al. 2000, Penner et al. 2003, Johnson et al. 2004, Ming et al. 2010).

3.5 Effects on precipitation

Figure 15 shows the mean precipitation rate during July-October together with the changes induced by the carbonaceous aerosols. The changes in precipitation rate are quite large in places, particularly around the NE part of the Gulf of Guinea and the adjacent land areas to the east. This area represents the southerly flank of the region of convective precipitation during the late boreal summer (Fig 15a) and is at the northerly limit of the strong aerosol-induced surface cooling (Fig. 12). Thus, the strong surface cooling appears to be limiting the extent of the ITCZ during this season, and there is evidence that the Atlantic ITCZ is moved northward (Fig. 15b). Weaker reductions in precipitation are also seen at the northern flank of the ITCZ too (Fig 15b). There are also increases in precipitation in the Arabian Peninsula (Fig 15b) but the model tends to produce way too much precipitation in this region compared with observations (Fig. 15a) reflecting a long term bias in CAM, and this signature should not be trusted.

4. Conclusion

In this paper we use the CAM 3.0 model with a slab ocean to conduct simulations to explore the regional direct and semi-direct effects of carbonaceous aerosols associated with biomass burning over southern Africa during the July-September dry season. In this region, burning over the southern African region generates large quantities of carbonaceous (both

564 organic and black carbon) aerosols, which are lofted by convection to altitudes up to 5 km and
565 then advected over the southeastern Atlantic Ocean where there are extensive low level clouds.
566 We adjusted the model aerosols using satellite observations and introduced a new approach to
567 quantifying the optical thickness of above-cloud aerosols. We neglected aerosol indirect effects
568 in this particular study.

569 Our primary findings are that the total TOA aerosol radiative effect of biomass buring
570 aerosols over the southern African/Atlantic region is significantly altered by the inclusion of
571 semi-direct effects. These semi-direct effects are primarily driven by changes in cloud cover and
572 to a lesser extent liquid water path over the ocean, and by changes in liquid water path over land.
573 The total TOA aerosol effect averaged over both land and ocean due to carbonaceous aerosols is
574 quite close to zero since there is a significant degree of cancellation of direct effects by semi-
575 direct effects by land and ocean effects that are of opposite sign. The TOA direct effect over the
576 ocean is strongly controlled by the mean low cloud cover in accordance with previous studies. In
577 the model we find that the sign of the TOA direct effect changes sign from negative to positive at
578 a cloud fraction of around 40-50% in accordance with previous observationally-based estimates
579 (Chand et al. 2009), which suggests a good degree of skill in the model representation of the
580 albedo of the clouds underlying the aerosol layers. Although the net forcing for the analyzed
581 region at TOA is near zero, the differing signatures over land and ocean can produce significant
582 changes in land/sea circulations.

583 The cloud changes responsible for the semi-direct effects are driven by (a) reductions in
584 near-surface temperature, (b) increases in free-tropospheric temperature, and (c) reduced large-
585 scale subsidence, all three of which are driven to first order by the aerosol direct effects. The
586 importance of surface cooling means that models not permitting a surface temperature response

587 (e.g. atmosphere-only models) will most likely underestimate the semi-direct effects. These
588 effects increase marine low cloud cover and thickness and reduce convection and its associated
589 liquid water over land. The results are sensitive to the parameterization of low clouds. Removing
590 the Klein and Hartmann diagnostic parameterization from the cloud scheme does change the
591 magnitude of the cloud responses but does not change their sign, which gives us some
592 confidence that the general nature of the results presented here is robust.

593 There also appear to be significant changes in the precipitation pattern driven by the
594 carbonaceous aerosols. Overall, precipitation over the African convective region is decreased in
595 our simulations, primarily through limitation of the extent of the convective region. Analyses
596 suggest that that much of the southern African biomass burning is anthropogenic and has
597 therefore likely increased somewhat contemporaneously with increases in sulfate aerosols in the
598 northern hemisphere (e.g. Ito and Penner, 2005). One prevailing view is that reductions in Sahel
599 precipitation over the second half of the 20th century may have been caused in part by increases
600 in sulfate aerosol which cooled the northern Atlantic thus driving the ITCZ southward. Our
601 results lead us to hypothesize that the increases in biomass burning aerosol may also play a
602 significant role in limiting the horizontal extent of the ITCZ and driving down the magnitude of
603 the convective precipitation in the northern African summer season. We plan to conduct further
604 model studies to explore this issue in future work.

605 Overall, the model results show the merits of conducting aerosol perturbation modeling
606 studies focusing on limited areas to complement global aerosol-climate assessments and highly
607 idealized process model studies.

608

609

Acknowledgements

The authors would like to thank Duli Chand for helpful suggestions and discussion which improved the paper. This work was supported by National Oceanographic and Atmospheric Administration Grant NA070AR4310282.

Appendix A

Derivation of equation [1]

$$\Delta F = F_{all}^{PD} - F_{all}^{NC}$$

defining and substituting $F_{all} = CF \cdot F_{CLDY} + (1 - CF) F_{CLR}$

$$\Delta F = [CF^{PD} \cdot F_{CLDY}^{PD} + (1 - CF^{PD}) F_{CLR}^{PD}] - [CF^{NC} \cdot F_{CLDY}^{NC} + (1 - CF^{NC}) F_{CLR}^{NC}]$$

Substituting $CF^{PD} = \overline{CF} + \frac{1}{2}\Delta CF$ and $CF^{NC} = \overline{CF} - \frac{1}{2}\Delta CF$

where $\Delta CF = CF^{PD} - CF^{NC}$ and $\overline{CF} = \frac{1}{2}(CF^{PD} + CF^{NC})$

$$\Delta F = (1 - \overline{CF})\Delta F_{CLR} + \overline{CF} \cdot \Delta F_{CLDY} + \frac{1}{2}\Delta CF[(F_{CLDY}^{PD} + F_{CLDY}^{NC}) - (F_{CLR}^{PD} + F_{CLDY}^{NC})]$$

substituting $2\overline{F}_{CLR} = (F_{CLR}^{PD} + F_{CLR}^{NC})$, $2\overline{F}_{CLDY} = (F_{CLDY}^{PD} + F_{CLDY}^{NC})$,

and $\Delta F_{CLDY} = \Delta F_{CLDY,Direct} - \Delta F_{CLDY,LWP}$

$$\Delta F = \{DRE_{CLR}(1 - \overline{CF})\} + \{\overline{CF} \cdot DRE_{CLDY}\} + \{\overline{CF} \cdot \Delta F_{CLDY,LWP}\} + \{\Delta CF(\overline{F}_{CLDY} - \overline{F}_{CLR})\}$$

where $DRE_{CLR} = \Delta F_{CLR}$ and $DRE_{CLDY} = \Delta F_{CLDY,Direct}$

630 ## References

631 Ackerman, A. S., Toon, O. B., Stevens, D. E., Heymsfield, A. J., Ramanathan, V. and Welton, E.
632 J., 2000: Reduction of tropical cloudiness by soot. *Science*, **288,** 1042–1047.

633 Allen, R.J and S.C. Sherwood. Aerosol-cloud semi-direct effect and land-sea temperature
634 contrast in a GCM. Geophysical Research Letters, vol. 37, L0880s, doi:
635 10.1029/2010GL042759, 2010.

636 Boville, B. A., P. J. Rasch, J. J. Hack, and J. R. McCaa, 2006: Representation of clouds and
637 precipitation processes in the Community Atmosphere Model Version 3 (CAM3). *J. Climate*,
638 **19**, 2184–2198.

639 Chand, D., T. L. Anderson, R. Wood, R. J. Charlson, Y. Hu, Z. Liu, and M. Vaughan.
640 Quantifying above-cloud aerosol using spaceborne lidar for improved understanding of
641 cloudy-sky direct climate forcing. Journal of Geophysical Research, vol. 113, D13206, doi:
642 10.1029/2007JD009433, 2008.

643 Chand D, R.Wood, T.L. Anderson, S.K. Satheesh, and R.J. Charlson. Satellite-derived direct
644 radiative effect of aerosols dependent on cloud cover. Letters, Nature Geoscience, vol.2 doi:
645 10.1038/NGEO437, 2009.

646 Chen, W.-T., Lee, Y.H., Adams, P.J., Nenes, A., and Seinfeld, J.H. (2010) Will black carbon
647 mitigation dampen aerosol indirect forcing?, *Geoph.Res.Let.*, **37**, L09801,
648 doi:10.1029/2010GL042886

649 Chýlek, P. & Coakley, J. A. Jr. Aerosol and climate. *Science,* **183**, 75_77 (1974).

650 Collins, W. D., P. J. Rasch, B. E. Eaton, B. V. Khattatov, J.-F. Lamarque, and C. S. Zender
651 (2001), Simulating aerosols using a chemical transport model with assimilation of satellite
652 aerosol retrievals: Methodology for INDOEX, *J. Geophys. Res.*, 106(D7), 7313–7336.

653 Collins, W. D, P. J. Rasch, B. A. Boville, J. J. Hack, J. R. McCaa, D. L. Williamson, J. T. Kiehl,
654 B. Briegleb, C. Bitz, S.-J. Lin, M. Zhang, and Y. Dai, 2004: Description of the NCAR
655 Community Atmospheric Model (CAM 3.0). NCAR/TN-464+STR, NCAR Technical Note.
656 National Center for Atmospheric Research, Boulder, USA.

657 Cook, J. and E.J. Highwood. Climate response to tropospheric absorbing aerosols in an
658 intermediate general-circulation model. Q. J. R. Meteorol. Soc. (2004), 130, pp. 175-191,
659 doi: 10.1256/qj.03.64.

660 Cooke, W., B. Koffi, and J.-M. Grégoire (1996), Seasonality of vegetation fires in Africa from
661 remote sensing data and application to a global chemistry model, J. Geophys. Res.,
662 101(D15), 21051-21065.

663 Gordon C. T., A. Rosati, R. Gudgel, 2000: Tropical sensitivity of a coupled model to specified
664 ISCCP low clouds. *J. Clim.,* **13**, 2239-2260.

665 Guan, H., B. Schmid, A. Bucholtz, and R. Bergstrom. Sensitivity of shortwave radiative flux
666 density, forcing, and heating rate to the aerosol vertical profile. Journal of Geophysical
667 Research, vol. 115, D06209, doi:10.1029/2009DJ012907, 2010.

668 Hansen, J., M. Sato, and R. Ruedy. Radiative forcing and climate response. Journal of
669 Geophysical Research, vol. 102, NO. D6, PAGES 6831-6864, 1997.

670 IPCC: Climate Change 2007: The Physical Science Basis, Contribution of Working Group I to
671 the Fourth Assessment Report of the Intergovernmental Panel on Climate Change, edited by:
672 Solomon, S., Qin, D., Manning, M., Chen, Z., Marquis, M. C., Avery, K. B., Tignor, M., and
673 Miller, H. L.

674 Ito, A., and J. E. Penner, 2005: Historical emissions of carbonaceous aerosols from biomass and
675 fossil fuel burning for the period 1870–2000, *Global Biogeochem. Cycles*, **19**, GB2028,
676 doi:10.1029/2004GB002374.

677 Johnson, B.T., K. P. Shine, and P.M. Foster, 2004: The semi-direct aerosol effect: Impact of
678 absorbing aerosols on marine stratocumulus. Q. J. R. Meteorol. Soc., 130, pp. 1407-1422,
679 doi: 10.1256/qj.03.61.

680 Kaufman, Y. J., L. A. Remer, D. Tanre, R. R. Li, R. Kleidman, S. Mattoo, R. Levy, T. Eck, B. N.
681 Holben, C. Ichoku, J. Martins, and I. Koren, 2005: A critical examination of the residual
682 cloud contamination and diurnal sampling effects on MODIS estimates of aerosol over
683 ocean. *IEEE Trans. Geosci. Remote Sens.*, **43** (12), 2886-2897.

684 Klein, S. A., and D. L. Hartmann, The seasonal cycle of low stratiform clouds, J. Climate, 6,
685 1587-1606, 1993.

686 Lau, W. K., M. K. Kim, K. M. Kim, Asian summer monsoon anomalies induced by aerosol
687 direct forcing: the role of the Tibetan Plateau. Clim. Dyn., 26, 855-864, 2006.

688 Lau, W. K M, Maeng-Ki Kim, Kyu-Myong Kim, and Woo-Seop Lee. Enhanced surface
689 warming and accelerated snow melt in the Himalayas and Tibetan Plateau induced by

absorbing aerosols. Environmental Research Letters, 5 (2010) 025204 (10pp), doi: 10.1088/1748-9326/5/2/025204.

Lau, K.-M. and K.-M. Kim. Observational relationships between aerosol and Asian monsoon rainfall, and circulation. Geophysical Research Letters, vol. 33, L21810, doi: 10.1029/2006GL027546, 2006.

Leahy, L. V., T. L. Anderson, T. F. Eck, and R. W. Bergstrom (2007), A synthesis of single scattering albedo of biomass burning aerosol over southern Africa during SAFARI 2000, Geophys. Res. Lett., 34, L12814, doi:10.1029/2007GL029697

Levine, Joel S., Wesley R. Coffer III, Donald R. Cahoon, JR., Edward L. Winstead. A Driver for Global Change, Environmenal Science and Technology, Volume 29, Number 3, pages 120A-125A.

Levy, R. C., L. A. Remer, S. Mattoo, E. F. Vermote, and Y. J. Kaufman (2007), Second-generation operational algorithm: Retrieval of aerosol properties over land from inversion of Moderate Resolution Imaging Spectroradiometer spectral reflectance, *J. Geophys. Res*., 112, D13211, doi:10.1029/2006JD007811.

Loeb, N.G., and N. Manalo-Smith, 2005: Top-of-atmosphere direct radiative effect of aerosols over global oceans from merged CERES and MODIS observations, *J. Climate*, 18, 3506-3526.

Ma, C.-C., C.R. Mechoso, A.W. Robertson and A. Arakawa, 1996: Peruvian stratus clouds and the tropical Pacific circulation: A coupled ocean-atmosphere GCM study. *J. Climate*, **9**, 1635-1645.

711 Matichuk, R. I., P. R. Colarco, J. A. Smith, and O. B. Toon (2007), Modeling the transport and
712 optical properties of smoke aerosols from African savanna fires during the Southern African
713 Regional Science Initiative campaign (SAFARI 2000), J. Geophys. Res., 112, D08203,
714 doi:10.1029/2006JD007528.

715 Ming, Y., V. Ramaswamy, and G. Persad (2010), Two opposing effects of absorbing aerosols on
716 global-mean precipitation, *Geophys. Res. Lett.*, 37, L13701, doi:10.1029/2010GL042895.

717 Morgan, M. G., P. J. Adams, and D. W. Keith. Elicitation of expert judgments of aerosol forcing.
718 Climate Change (2006) 75: 195-214, doi: 10.1007/s10584-005-9025-y.

719 Penner, J. E., S. Y. Zhang, and C. C. Chuang, Soot and smoke aerosol may not warm climate, *J.*
720 *Geophys. Res*., **108**(D21), 4657, doi:10.1029/2003JD003409, 2003.

721 Ramanathan, V. and Carmichael, G. Global and regional climate changes due to black carbon.
722 *Nature Geosci*. 1, 221-227, (2008).

723 Rasch, P. J., N. M. Mahowald, and B. E. Eaton, Representations of transport, convection, and
724 the hydrologic cycle in chemical transport models: Implications for the modeling of short-lived
725 and soluble species, *J. Geophys. Res*., 102, 28127–28138, 1997.

726 Rasch, P. J., W. D. Collins, and B. E. Eaton (2001), Understanding the Indian Ocean Experiment
727 (INDOEX) aerosol distributions with an aerosol assimilation, *J. Geophys. Res.*, 106(D7),
728 7337–7355.

729 Remer, L. A., et al. (2005), The MODIS aerosol algorithm, products, and validation, *J. Atmos.*
730 *Sci*., 62(4), 947– 973.

731 Schulz, M. et al. Radiative forcing by aerosols as derived from the AeroCom present-day and
732 pre-industrial simulations. Atmos. Chem. Phys. 6, 5225-5246, 2006.

733 Sud, Y.C., E. Wilcox, W. K.-M. Lau, G. K. Walker, X.-H. Liu, A. Nenes, D. Lee, K.-M. Kim, Y.
734 Zhou, and P.S. Bhattacherjee. Sensitivity of boreal-summer circulation and precipitation to
735 atmospheric aerosols in selected regions – Part 1: Africa and India. Ann. Geophys., 27, 3989-
736 4007, 2009.

737 Richter, I. and C. R. Mechoso, 2004: Orographic influences on the annual cycle of Namibian
738 stratocumulus clouds. *Geophys. Res. Lett.*, 31, L24108.

739 Richter, I. and C. R. Mechoso, 2006: Orographic Influences on Subtropical Stratocumulus. *J. Atmos.*
740 *Sci.*, 63, 2585-2601.

741 Takahashi, K. and D. S. Battisti, 2007: Processes controlling the mean tropical Pacific
742 precipitation pattern. Part I: The Andes and the eastern Pacific ITCZ. *J. Climate*, **20**:3434–
743 3451.

744 Wood, R., and C. S. Bretherton, 2006: On the relationship between stratiform low cloud cover
745 and lower-tropospheric stability**,** *J. Clim.*, **19**, 6425-6432.

746 Wood R., and Hartmann, D. L., 2006: Spatial variability of liquid water path in marine low
747 cloud: The importance of mesoscale cellular convection. *J.Clim.,* **19**,1748-1764.

748 Yoshimori, M., and A. J. Broccoli (2008), Equilibrium response of an atmosphere-mixed layer
749 ocean model to different radiative forcing agents: Global and zonal mean response, *J. Clim*.,
750 21, 4399–4423.

Figure Captions

Figure 1: Change in AOD between simulation with and without carbonaceous. The dashed box represents the region where carbonaceous aerosol mass is modified.

Figure 2: Top row: July-October mean AOD at 500 nm (a) for all-sky conditions from CAM (nominally at 500 nm); (b) for clear-sky conditions from MODIS; (c) for aerosol layers above clouds from CALIPSO. Bottom row: (d) the difference in AOD between CAM with and without carbonaceous aerosols; (e) the MODIS fine mode fraction AOD for clear-sky conditions.

Figure 3: Observed mean aerosol optical depth (ordinate, red circles for MODIS fine mode AOD, and blue circles for CALIPSO above-cloud AOD) plotted as a function of the mean AOD used in CAM due to carbonaceous aerosols only. Each point represents a mean over a 5×5° region. Filled circles indicate locations over ocean, open circles locations over land. The dashed line shows the one-to-one line.

Figure 4: (a) Longitude-height cross section of July-October mean cloud fraction (colored contour) and mixing ratio of total carbonaceous aerosols (dashed line) from the CAM PD simulation, meridionally averaged over 0°-20°S. Note that the mean longitude of the southern African coastline is 12°E. (b) vertical profiles of cloud fraction and mixing ratio of total carbonaceous aerosols averaged over ocean only from (0°-20°S, 20°W-30°E).

Figure 5: Radiative forcing terms at TOA(left column, a-e), Surface(middle column, f-j), and Atmosphere (right colu1mn, k-o); first row(a,f,k): TermD1, second row(b,g,l): Term D2, third row(c,h,m): Term S1, fourth row(d,i,j): Term S2, fifth row(e,j,o): Sum of the four terms. Note that the different color scale is used for each column.

Figure 6: Total direct radiative forcing efficiency ($Wm^{-2}\tau^{-1}$), (a) at the top of atmosphere (TOA); (b) at the surface; (c) for the atmosphere.

Figure 7: Mean low cloud fraction against total direct RFE at atmosphere; colored by whether cloud layer is above (red) or below (blue) the aerosol layer

776 Figure 8: Surface, atmospheric, and TOA direct RFE from the model against the mean low cloud
777 fraction over (a) land; (b) ocean. The critical low cloud fractions CF* where the sign of the TOA
778 direct effect changes from negative to positive are shown.

779 Figure 9: Total cloud fraction vs. weighted mean aerosol SSA; black line showing the derived
780 cloud critical fraction line; positive (blue) and negative (red) total direct RFE at TOA; the size of
781 circles indicates the magnitude of the forcing

782 Fig. 10: (a) Low cloud cover (clouds at and below 700 hPa) for the simulation with carbonaceous
783 aerosols; (b) the change in low cloud cover between PD and NC simulations (with and without
784 carbonaceous aerosols); (c) high cloud cover (clouds above 700 hPa), and (d) change in high
785 cloud cover (PD-NC); (e) cloud liquid water path, and (f) change in liquid water path (PD-NC).

786 Fig 11: Changes (PD – NC) in low cloud fraction against changes in LTS over the ocean, for
787 standard run (red); CLDMOD2 (blue); and expected low cloud cover change from the Klein line
788 (dashed black line).

789 Figure 12: Change in surface air temperature between PD and NC runs. Strong cooling is
790 observed throughout the region with strong negative radiative effect at the surface (see Fig. 5j).

791 Figure 13: Means and changes (PD-NC) of (a) potential temperature, (b) relative humidity RH,
792 (c) cloud fraction, and (d) vertical velocity, for a region (8-18°S, 0-10°E) over the ocean with large
793 cloud cover changes (see Fig. 10).

794 Figure 14: Meridional cross sections (averaged over 0-20°S as in Fig. 4) showing changes in low
795 clouds (colored contours), change in RH (solid lines showing positive changes and dashed lines
796 showing negative changes).

797 Figure 15: (a) Mean precipitation rate during July-October, and (b) difference (PD-NC) in
798 precipitation caused by carbonaceous aerosols.

799

Tables

Table 1: Total cloud cover, radiative effects at the TOA, surface, and atmosphere, and their contributing terms (D1, D2, S1 and S2) averaged over 20°W-50°E, 10°N-30°S, given for the land and ocean separately, and for both land and ocean together. The column σ* gives the standard deviation over space. An estimate of the uncertainty in the terms can be obtained from the difference between the sum of four terms and the model output total forcing $(\Delta F^{net}_{model} - \Delta F^{net}_{calculated})$. This error is less than 0.1 W m^{-2} for the TOA and surface effects, and slightly higher for the atmospheric effects.

Variable		Land			Ocean			Both land and ocean		
		mean	median	σ*	mean	median	σ*	Mean	median	σ*
$\overline{CF}_{total}$		0.488	0.510	0.265	0.533	0.507	0.118	0.501	0.494	0.195
ΔCF_{total}		0.003	0.004	0.015	0.020	0.017	0.025	0.011	0.009	0.023
TOA [W m^{-2}]	Term D1	-0.80	-0.46	0.93	-1.36	-1.13	0.77	-1.15	-0.95	0.90
	Term D2	0.98	0.80	0.90	2.30	1.03	3.46	1.56	0.87	2.48
	Term S1	1.71	1.04	2.72	-0.68	-0.50	2.44	0.32	0.22	2.84
	Term S2	-0.41	-0.31	1.17	-1.93	-1.45	2.46	-1.08	-0.69	2.04
	Sum of all terms	1.48	1.27	2.78	-1.67	-1.63	2.80	-0.34	-0.41	3.19
Surface	Term D1	-9.27	-8.65	7.22	-4.50	-3.88	2.53	-6.64	-4.83	5.66
	Term D2	-3.81	-2.74	3.48	-3.17	-2.40	2.61	-3.39	-2.40	3.13
	Term S1	1.78	1.07	3.05	-0.88	-0.60	2.85	0.22	0.12	3.25
	Term S2	-0.46	-0.31	1.26	-2.29	-1.65	2.94	-1.26	-0.77	2.38
	Sum of all terms	-11.76	-11.87	7.71	-10.84	-9.32	7.66	-11.06	-10.24	7.56
Atmosphere	Term D1	8.47	7.30	6.97	3.14	2.80	1.79	5.49	3.52	5.43
	Term D2	4.80	3.72	3.21	5.48	3.48	5.51	4.95	3.50	4.40
	Term S1	-0.07	-0.003	0.36	0.21	0.13	0.44	0.10	0.07	0.43
	Term S2	0.04	0.03	0.09	0.35	0.21	0.49	0.18	0.06	0.36
	Sum of all terms	13.24	11.92	7.50	9.17	6.94	7.29	10.72	8.48	7.54

Table 2: Radiative forcing efficiency [20W-50E, 10N-30S]

Radiative forcing efficiency ($Wm^{-2}\tau^{-1}$)		Over land			Over ocean		
		mean	median	Standard deviation over space	mean	median	Standard deviation over space
Direct	TOA	3.63	2.05	7.77	1.97	-1.58	12.40
	Atmosphere	61.61	60.59	7.81	60.18	57.64	11.10
	Surface	-57.95	-58.58	11.74	-58.18	-59.68	9.20
Semi-direct	TOA	6.62	4.02	24.42	-23.42	-17.42	38.05
	Atmosphere	0.052	0.26	4.49	3.92	3.34	5.38
	Surface	6.56	3.88	27.71	-27.35	-20.88	42.79
Total	TOA	10.25	5.78	22.42	-21.44	-14.72	35.37
	Atmosphere	61.66	61.92	9.18	64.10	60.28	14.49
	Surface	-51.39	-57.66	28.91	-85.54	-77.12	42.91

Table 3: Radiative forcing and cloud fraction comparison with (CONTROL) and without (CLDMOD2) the Klein and Hartmann stability-based diagnostic parameterization of marine stratus clouds [30°W-50°E, 10°N-30°S]. The column headed r^2 shows the spatial correlation between a particular variable for the CONTROL and CLDMOD2 simulations respectively. Thus, a value $r^2=1$ indicates that the effect of changing the low cloud parameterization does not influence the spatial pattern of the variable.

Variable		Over land			Over ocean		
		CONTROL	CLDMOD2	r^2	CONTROL	CLDMOD2	r^2
$\overline{CF_{low}}$		0.171	0.178	1.00	0.470	0.373	0.73
ΔCF_{low}		0.003	0.013	0.61	0.023	0.012	0.75
$\overline{CF_{total}}$		0.488	0.493	1.00	0.533	0.443	0.70
ΔCF_{total}		0.003	0.002	0.54	0.020	0.008	0.68
$\overline{CLDLWP}$		78.28	79.70	1.00	68.99	66.08	0.98
$\Delta CLDLWP$		-3.80	-1.44	0.71	2.69	1.28	0.69
$\overline{LTS}$		8.05	8.24	1.00	18.42	18.57	0.99
ΔLTS		0.50	0.54	0.78	0.47	0.44	0.99
ΔAOD		0.104	0.105	1.00	0.069	0.069	1.00
Top of Atmosphere	Term D1 (Wm^{-2})	-0.80	-0.82	1.00	-1.36	-1.66	0.92
	Term D2 (Wm^{-2})	0.98	1.11	0.96	2.30	2.27	0.99
	Term S1 (Wm^{-2})	1.71	0.95	0.70	-0.68	-0.38	0.65
	Term S2 (Wm^{-2})	-0.41	-0.51	0.38	-1.93	-0.99	0.72
	Sum of all terms (Wm^{-2})	1.48	0.73	0.68	-1.67	-0.76	0.60
	Error (Wm^{-2})	0.03	0.08	0.37	0.005	0.003	0.84
Surface	Term D1 (Wm^{-2})	-9.27	-9.16	1.00	-4.50	-5.64	0.90
	Term D2 (Wm^{-2})	-3.81	-3.85	1.00	-3.17	-2.24	0.84
	Term S1 (Wm^{-2})	1.78	0.84	0.70	-0.88	-0.53	0.67
	Term S2 (Wm^{-2})	-0.46	-0.57	0.36	-2.29	-1.17	0.74
	Sum of all terms (Wm^{-2})	-11.76	-12.74	0.95	-10.84	-9.58	0.92
	Error (Wm^{-2})	0.034	-0.030	0.18	-0.047	-0.038	0.77
Atmosphere	Term D1 (Wm^{-2})	8.47	8.34	1.00	3.14	3.97	0.90
	Term D2 (Wm^{-2})	4.80	4.96	1.00	5.48	4.52	0.97
	Term S1 (Wm^{-2})	-0.07	0.11	0.61	0.21	0.15	0.77
	Term S2 (Wm^{-2})	0.04	0.07	0.20	0.35	0.18	0.81
	Sum of all terms (Wm^{-2})	13.24	13.47	1.00	9.17	8.82	1.00
	Error (Wm^{-2})	-0.011	0.10	0.51	0.05	0.04	0.77

Figures

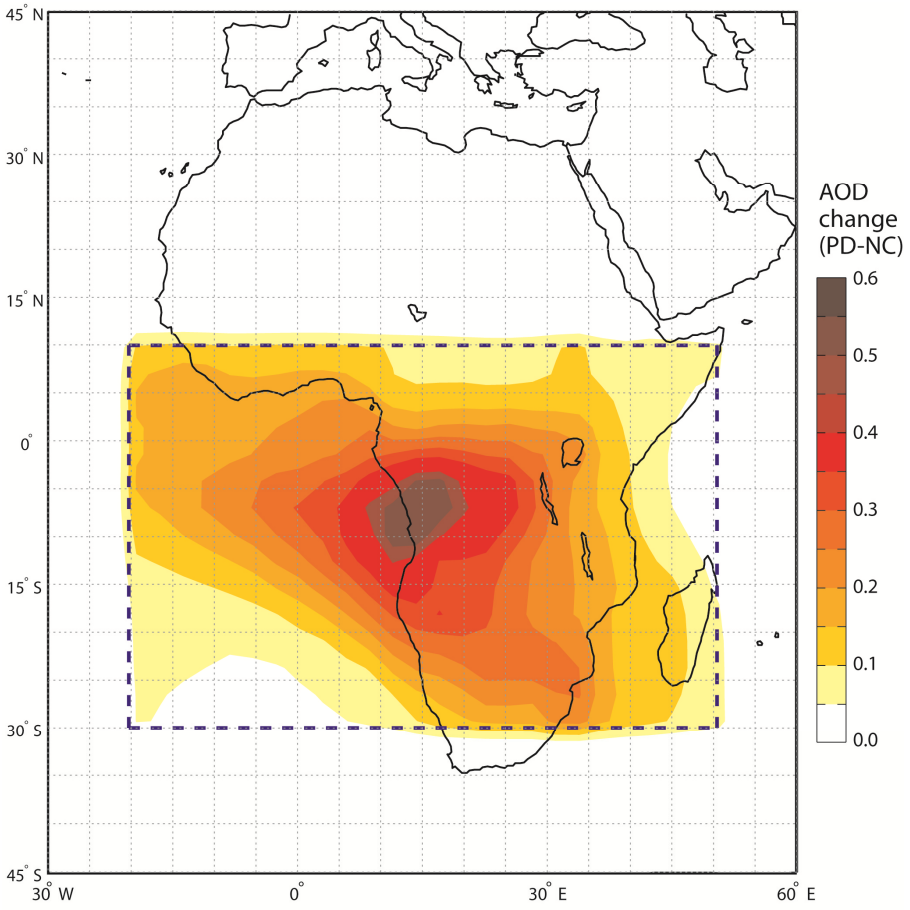

Figure 1: Change in AOD between simulation with and without carbonaceous. The dashed box represents the region where carbonaceous aerosol mass is modified.

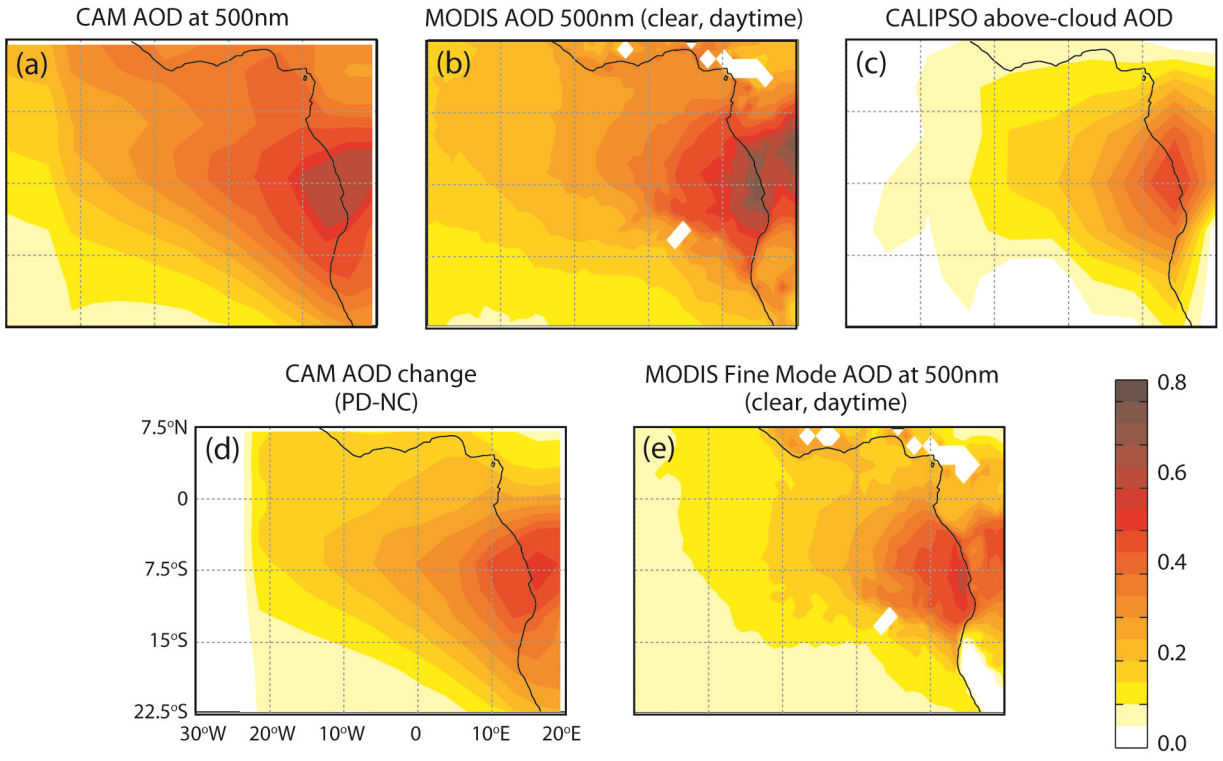

828

829 Figure 2: Top row: July-October mean AOD at 500 nm (a) for all-sky conditions from CAM
830 (nominally at 500 nm); (b) for clear-sky conditions from MODIS; (c) for aerosol layers above
831 clouds from CALIPSO. Bottom row: (d) the difference in AOD between CAM with and without
832 carbonaceous aerosols; (e) the MODIS fine mode fraction AOD for clear-sky conditions.

833

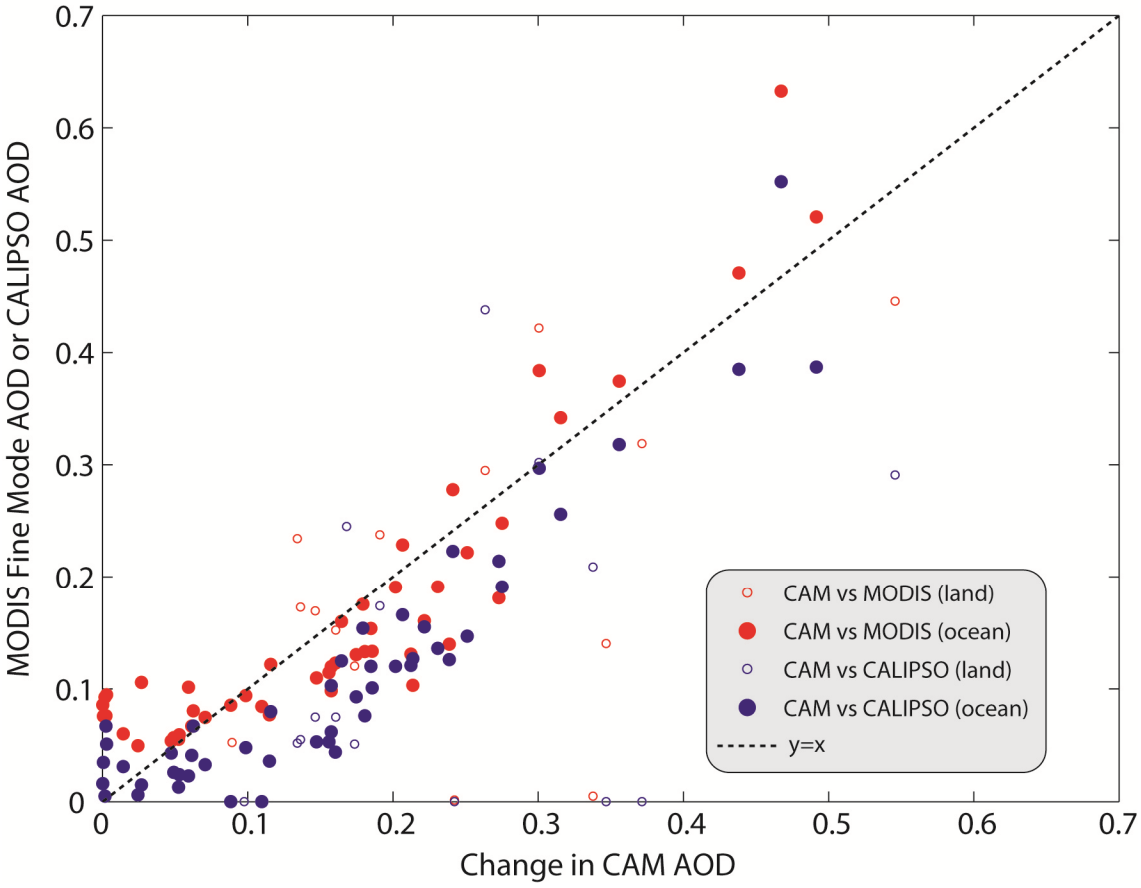

Figure 3: Observed mean aerosol optical depth (ordinate, red circles for MODIS fine mode AOD, and blue circles for CALIPSO above-cloud AOD) plotted as a function of the mean AOD used in CAM due to carbonaceous aerosols only. Each point represents a mean over a 5×5° region. Filled circles indicate locations over ocean, open circles locations over land. The dashed line shows the one-to-one line.

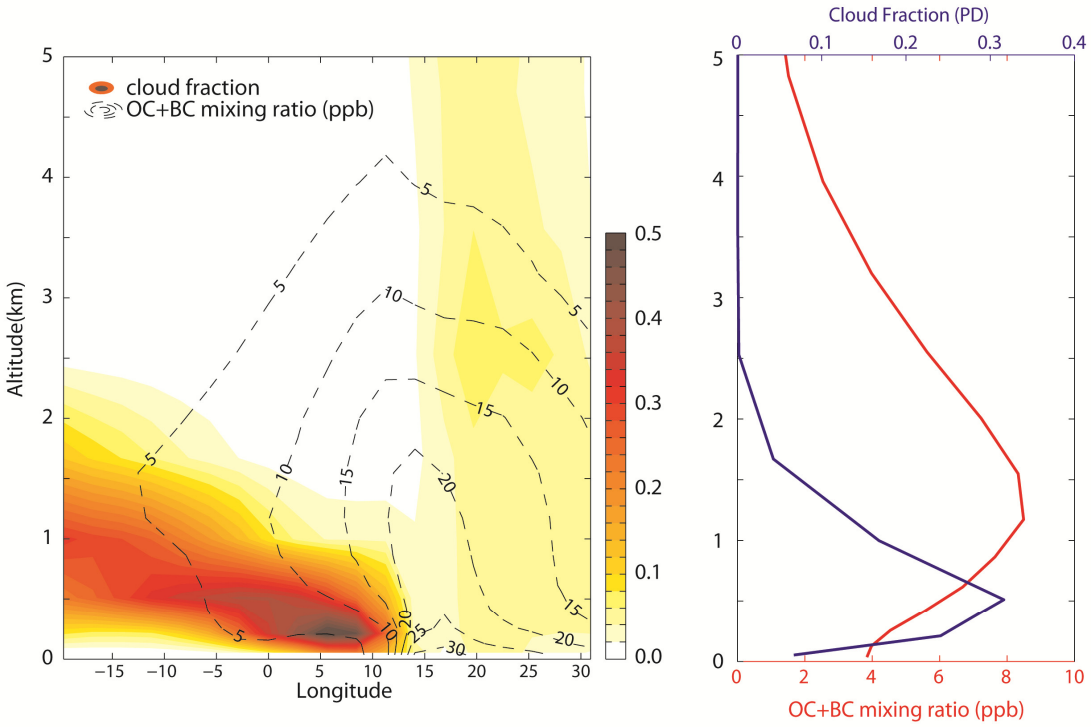

843

844 Figure 4: (a) Longitude-height cross section of July-October mean cloud fraction (colored
845 contour) and mixing ratio of total carbonaceous aerosols (dashed line) from the CAM PD
846 simulation, meridionally averaged over 0°-20°S. Note that the mean longitude of the southern
847 African coastline is 12°E. (b) vertical profiles of cloud fraction and mixing ratio of total
848 carbonaceous aerosols averaged over ocean only from (0°-20°S, 20°W-30°E).

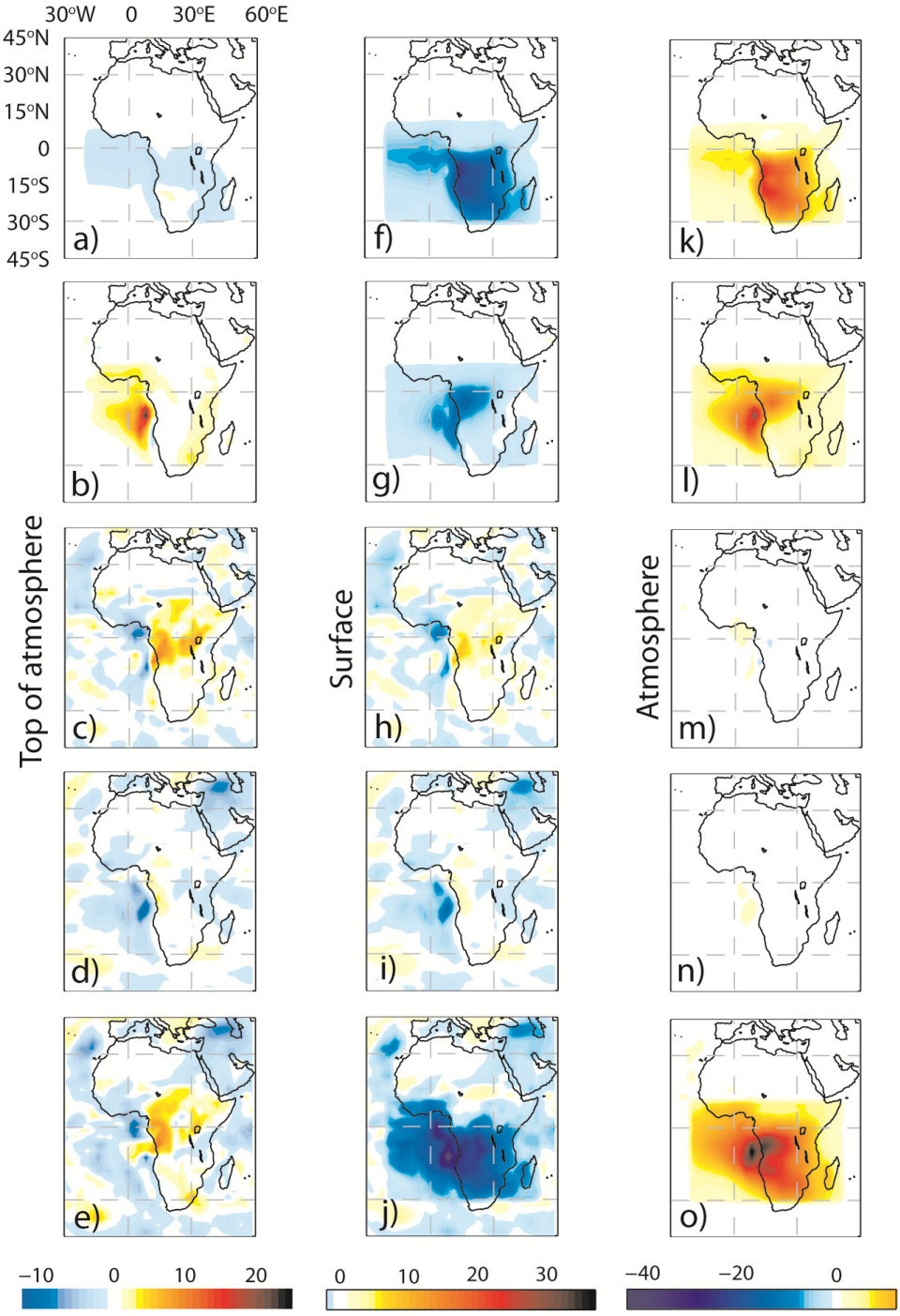

849

850 Figure 5: Radiative forcing terms at TOA(left column, a-e), Surface(middle column, f-j), and Atmosphere
851 (right colu1mn, k-o); first row(a,f,k): TermD1, second row(b,g,l): Term D2, third row(c,h,m): Term S1,
852 fourth row(d,i,j): Term S2, fifth row(e,j,o): Sum of the four terms. Note that the different color scale is
853 used for each column.

854

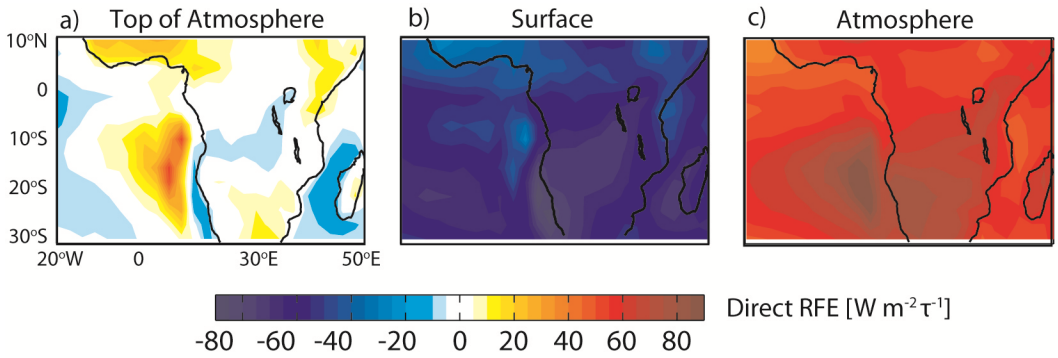

855

856 Figure 6: Total direct radiative forcing efficiency ($Wm^{-2}\tau^{-1}$), (a) at the top of atmosphere (TOA);

857 (b) at the surface; (c) for the atmosphere.

858

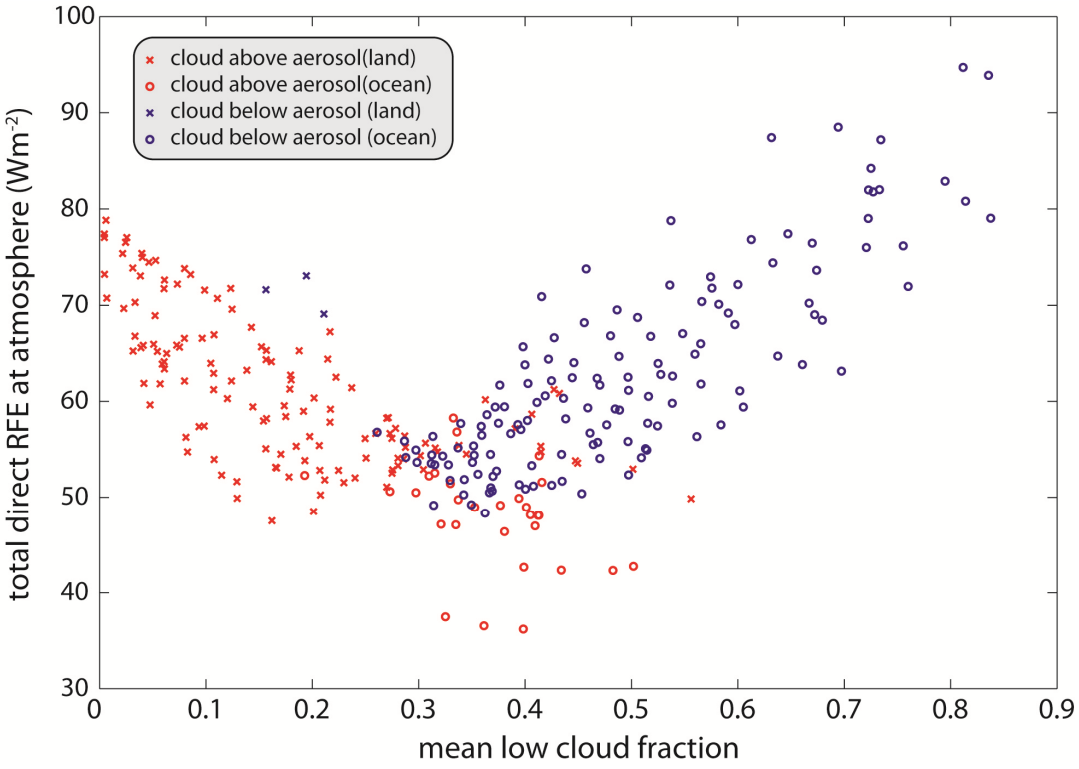

Figure 7: Mean low cloud fraction against total direct RFE at atmosphere; colored by whether cloud layer is above (red) or below (blue) the aerosol layer

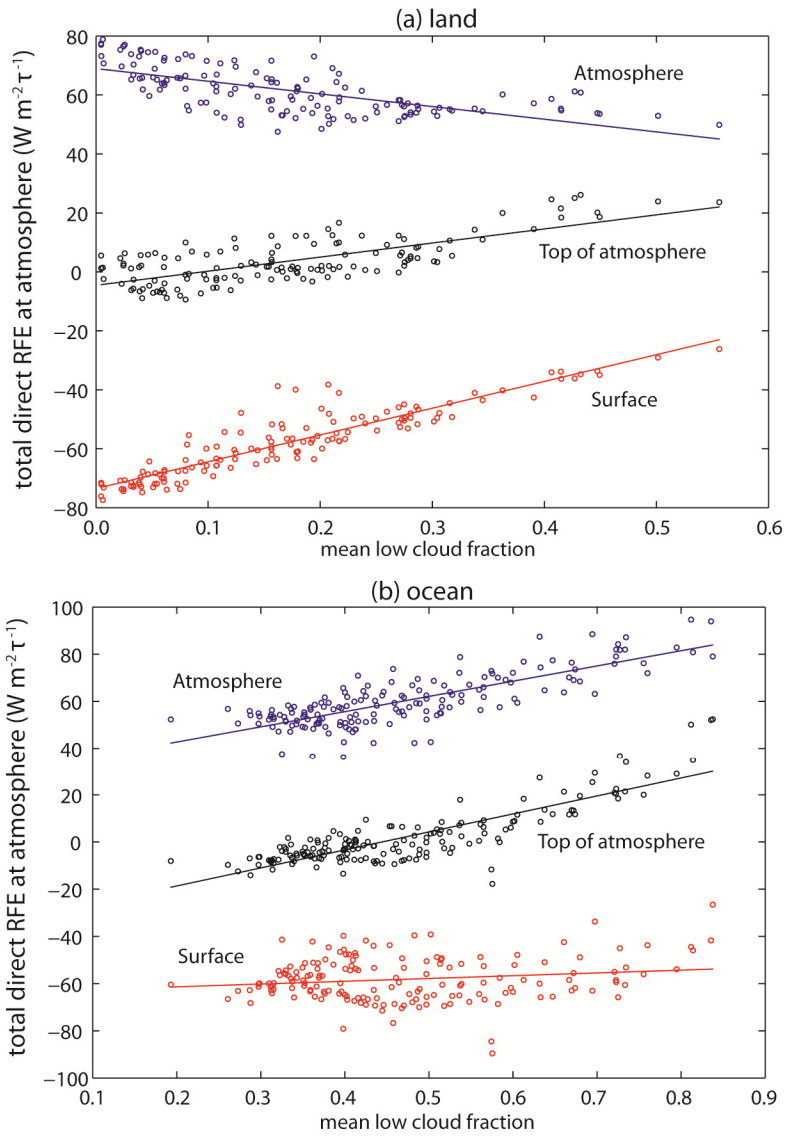

Figure 8: Surface, atmospheric, and TOA direct RFE from the model against the mean low cloud fraction over (a) land; (b) ocean. The critical low cloud fractions CF* where the sign of the TOA direct effect changes from negative to positive are shown.

886

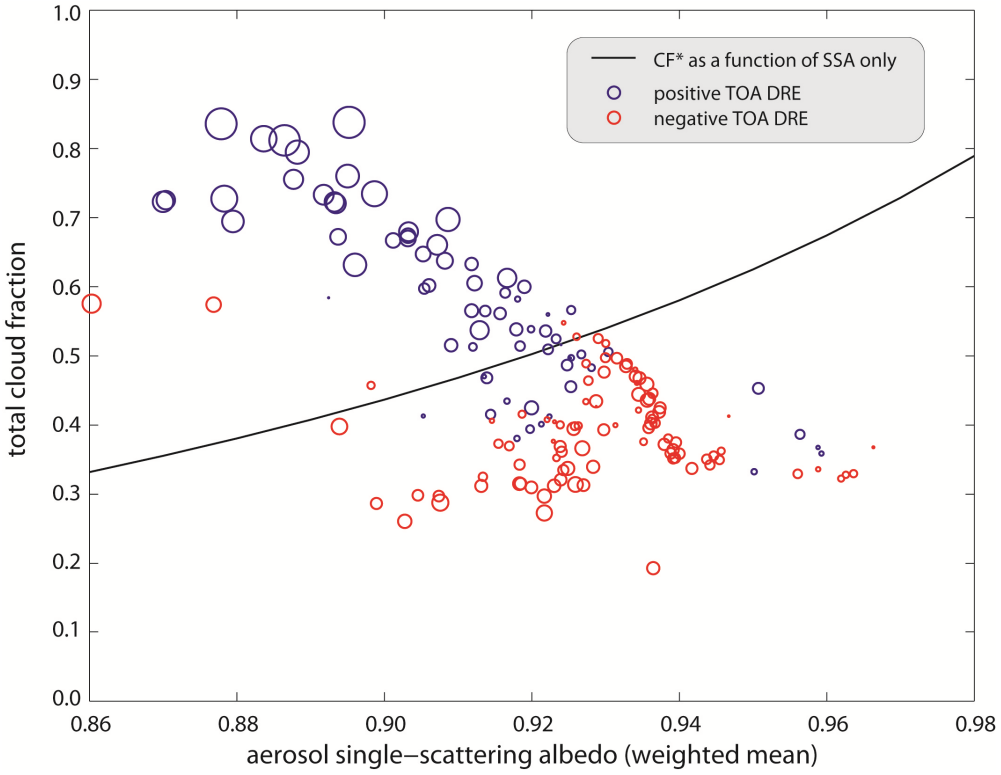

887

888 Figure 9: Total cloud fraction vs. weighted mean aerosol SSA; black line showing the derived

889 cloud critical fraction line; positive (blue) and negative (red) total direct RFE at TOA; the size of

890 circles indicates the magnitude of the forcing

891

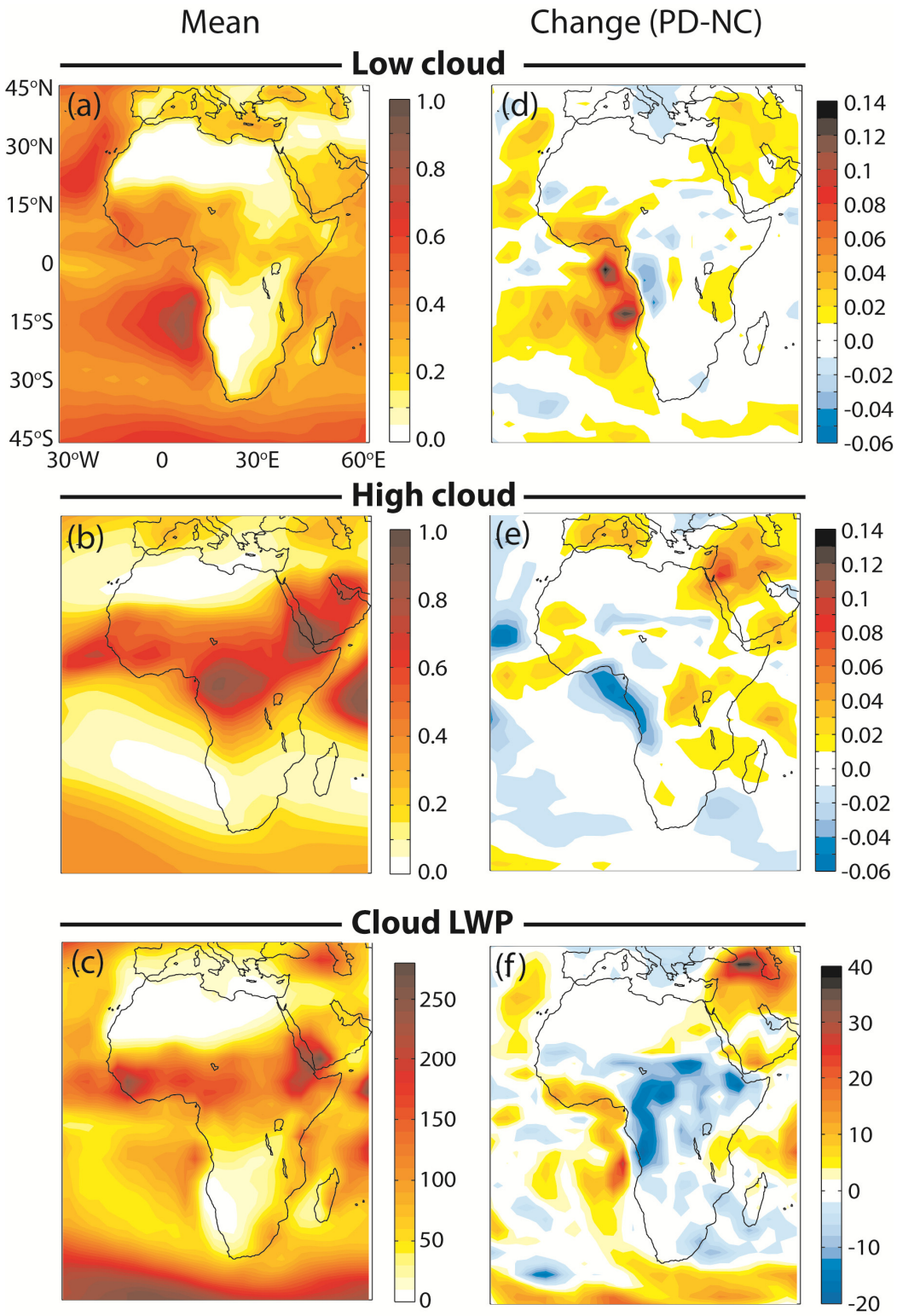

Fig. 10: (a) Low cloud cover (clouds at and below 700 hPa) for the simulation with carbonaceous aerosols; (b) the change in low cloud cover between PD and NC simulations (with and without carbonaceous aerosols); (c) high cloud cover (clouds above 700 hPa), and (d) change in high cloud cover (PD-NC); (e) cloud liquid water path, and (f) change in liquid water path (PD-NC).

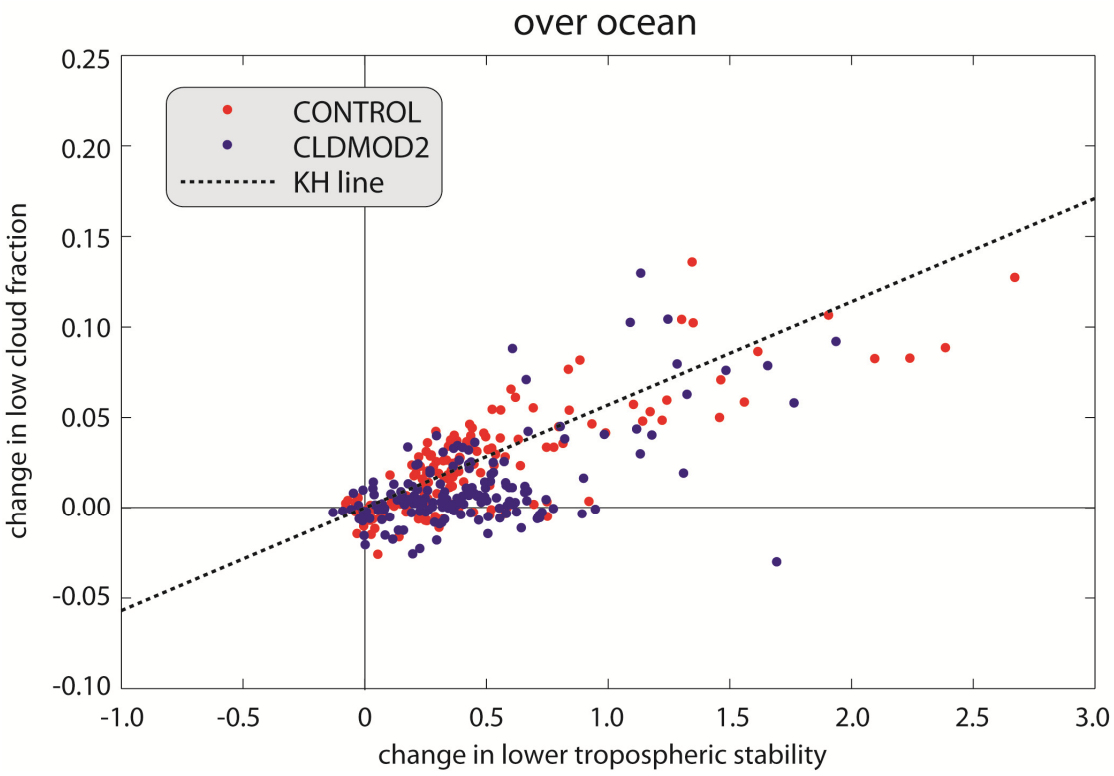

Fig 11: Changes (PD – NC) in low cloud fraction against changes in LTS over the ocean, for standard run (red); CLDMOD2 (blue); and expected low cloud cover change from the Klein line (dashed black line).

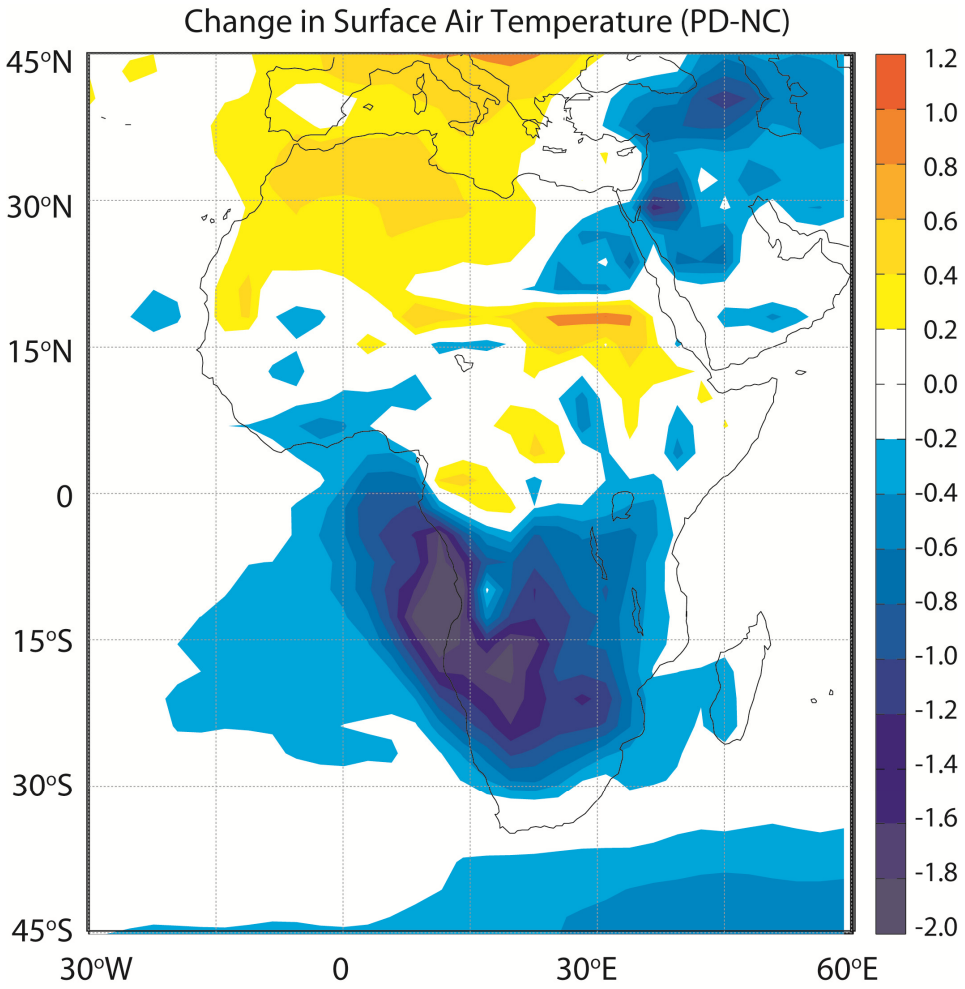

904

905 Figure 12: Change in surface air temperature between PD and NC runs. Strong cooling is

906 observed throughout the region with strong negative radiative effect at the surface (see Fig. 5j).

907

908

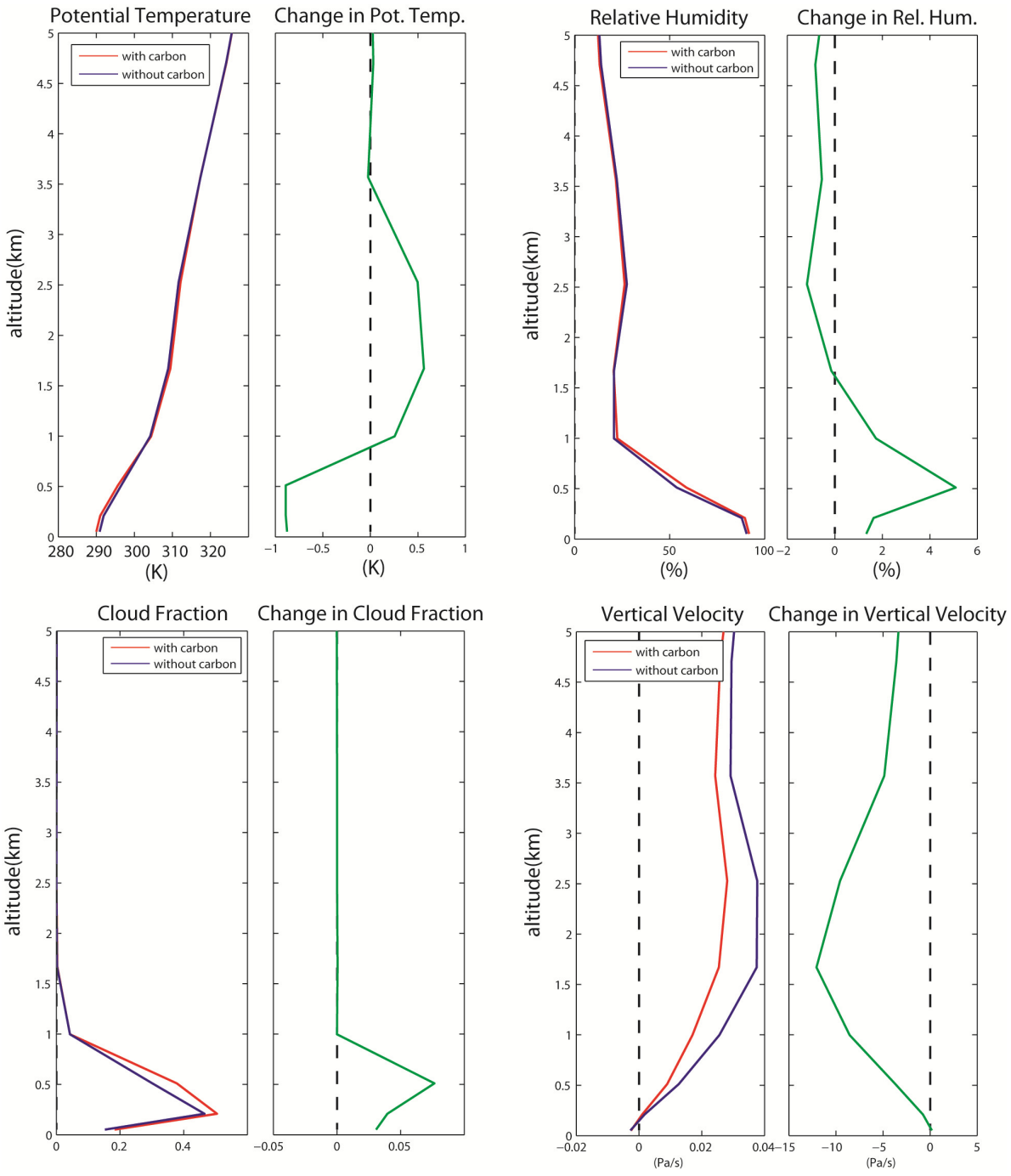

909

910 Figure 13: Means and changes (PD-NC) of (a) potential temperature, (b) relative

911 humidity RH, (c) cloud fraction, and (d) vertical velocity, for a region (8-18°S, 0-10°E) over the

912 ocean with large cloud cover changes (see Fig. 10).

913

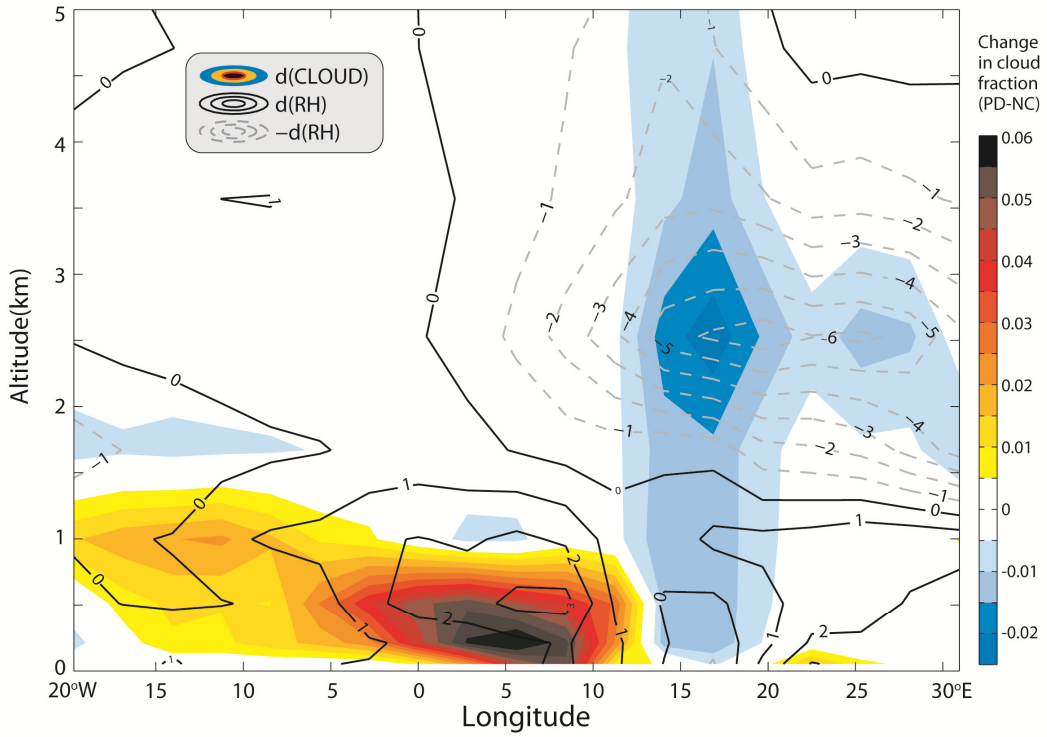

914

915 Figure 14: Meridional cross sections (averaged over 0-20°S as in Fig. 4) showing

916 changes in low clouds (colored contours), change in RH (solid lines showing positive changes

917 and dashed lines showing negative changes).

918

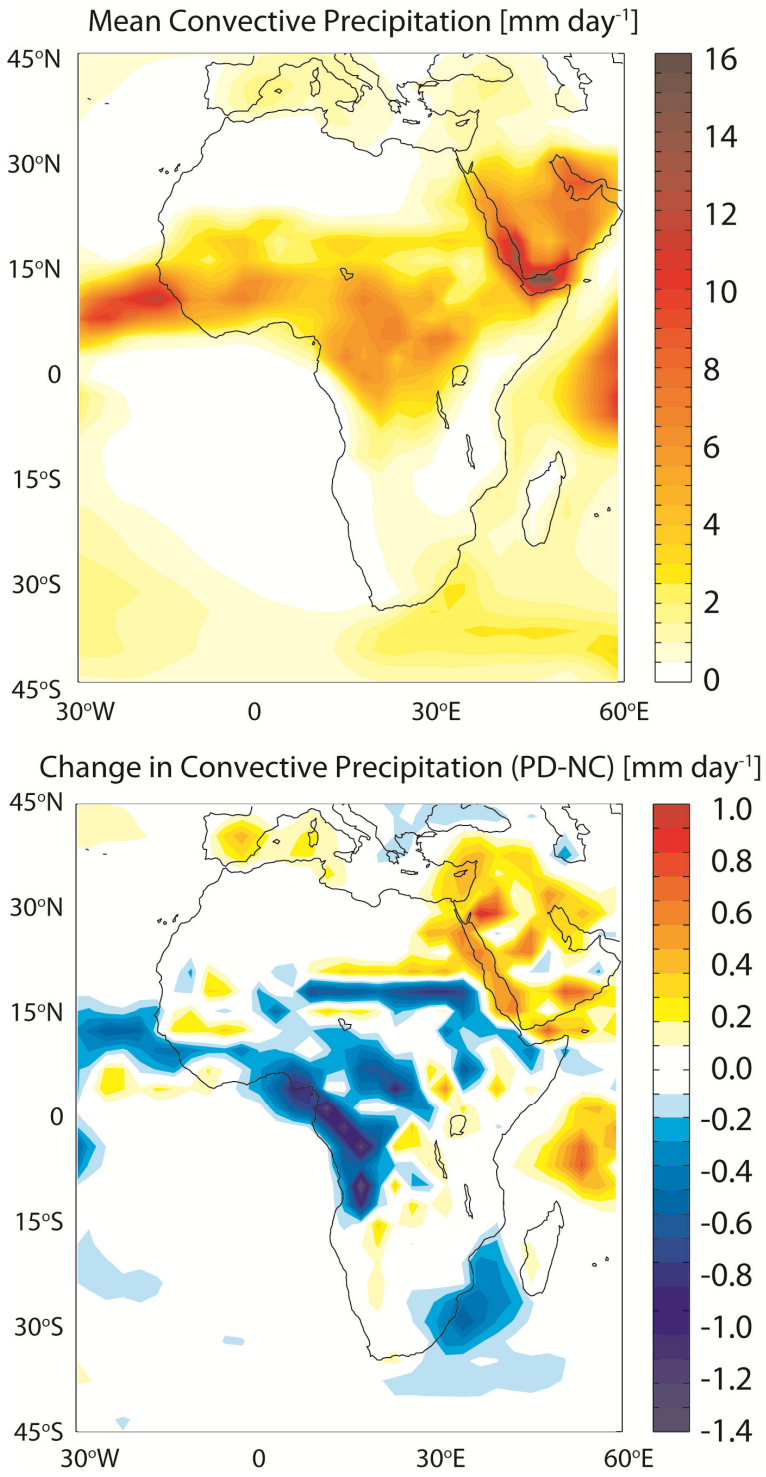

919

920 Figure 15: (a) Mean precipitation rate during July-October, and (b) difference (PD-NC) in
921 precipitation caused by carbonaceous aerosols.

922